Niche-selective inhibition of pathogenic Th17 cells by targeting metabolic redundancy

Lin Wu[1,3,7], Kate E.R. Hollinshead[2], Yuhan Hao[3,4], Christy Au[1,5], Lina Kroehling[1], Charles Ng[1], Woan-Yu Lin[1], Dayi Li[1], Hernandez Moura Silva[1], Jong Shin[6], Juan J. Lafaille[1,6], Richard Possemato[6], Michael E. Pacold[2], Thales Papagiannakopoulos[6], Alec C. Kimmelman[2], Rahul Satija[3,4], Dan R. Littman[1,5,6,7,8]

[1]The Kimmel Center for Biology and Medicine of the Skirball Institute, New York University School of Medicine, New York, NY, USA; [2]Department of Radiation Oncology and Perlmutter Cancer Center, New York University School of Medicine, New York, NY, USA; [3]New York Genome Center, New York, NY, USA; [4]Center for Genomics and Systems Biology, New York University, New York, NY, USA; [5]Howard Hughes Medical Institute, New York, NY, USA; [6]Department of Pathology, New York University School of Medicine, New York, NY, USA; [7]Corresponding Authors; [8]Lead Contact.

Lead Contact: dan.littman@med.nyu.edu

Correspondence: lin.wu@med.nyu.edu and dan.littman@med.nyu.edu

Key words: Autoimmunity, metabolic plasticity, hypoxia, glycolysis, CRISPR, OXPHOS, inflammation, segmented filamentous bacteria, EAE, colitis

Summary

Targeting glycolysis has been considered therapeutically intractable owing to its essential housekeeping role. However, the context-dependent requirement for individual glycolytic steps has not been fully explored. We show that CRISPR-mediated targeting of glycolysis in T cells in mice results in global loss of Th17 cells, whereas deficiency of the glycolytic enzyme glucose phosphate isomerase (Gpi1) selectively eliminates inflammatory encephalitogenic and colitogenic Th17 cells, without substantially affecting homeostatic microbiota-specific Th17 cells. In homeostatic Th17 cells, partial blockade of glycolysis upon *Gpi1* inactivation was compensated by pentose phosphate pathway flux and increased mitochondrial respiration. In contrast, inflammatory Th17 cells experience a hypoxic microenvironment known to limit mitochondrial respiration, which is incompatible with loss of *Gpi1*. Our study suggests that inhibiting glycolysis by targeting Gpi1 could be an effective therapeutic strategy with minimum toxicity for Th17-mediated autoimmune diseases, and, more generally, that metabolic redundancies can be exploited for selective targeting of disease processes.

41 **Introduction**

42

43 Cellular metabolism is a dynamic process that supports all aspects of the cell's activities. It
44 is orchestrated by more than 2000 metabolic enzymes organized into pathways that are
45 specialized for processing and producing distinct metabolites. Multiple metabolites are shared by
46 different pathways, serving as nodes in a complex network with many redundant elements. A
47 well-appreciated example of metabolic plasticity is the generation of ATP by either glycolysis or
48 by mitochondrial oxidative phosphorylation (OXPHOS), making the two processes partially
49 redundant despite having other non-redundant functions (O'Neill et al., 2016). Here, we explore
50 metabolic plasticity in the context of T cell function and microenvironment, and the consequence
51 of limiting that plasticity by inhibiting specific metabolic enzymes.

52 Th17 cells are a subset of $CD4^+$ T cells whose differentiation is governed by the
53 transcription factor RORγt, which regulates the expression of the signature IL-17 cytokines
54 (Ivanov et al., 2006). Under homeostatic conditions, Th17 cells typically reside at mucosal
55 surfaces where they provide protection from pathogenic bacteria and fungi and also regulate the
56 composition of the microbiota (Kumar et al., 2016; Mao et al., 2018; Milner and Holland, 2013;
57 Okada et al., 2015; Puel et al., 2011). However, under conditions that favor inflammatory
58 processes, Th17 cells can adopt a pro-inflammatory program that promotes autoimmune
59 diseases, including inflammatory bowel disease (Hue et al., 2006; Kullberg et al., 2006),
60 psoriasis (Piskin et al., 2006; Zheng et al., 2007) and diverse forms of arthritis (Hirota et al.,
61 2007; Murphy et al., 2003; Nakae et al., 2003a; Nakae et al., 2003b). This program is dependent
62 on IL-23 and is typically marked by the additional expression of T-bet and IFN-γ (Ahern et al.,
63 2010; Cua et al., 2003; Hirota et al., 2011; Morrison et al., 2013). The Th17 pathway has been
64 targeted with neutralizing antibodies specific for IL-17A or IL-23 to effectively treat psoriasis,

ulcerative colitis, Crohn's disease, and some forms of arthritis (Fotiadou et al., 2018; Hanzel and D'Haens, 2020; Langley et al., 2018; Moschen et al., 2019; Pariser et al., 2018; Tahir, 2018; Wang et al., 2017), but these therapies inevitably expose patients to potential fungal and bacterial infections, as they also inhibit homeostatic Th17 cell functions. In this study, we aimed to identify genes and pathways that are required for the function of inflammatory pathogenic Th17 cells, but are dispensable for homeostatic Th17 cells, which may enable the selective therapeutic targeting of pathogenic Th17 cells.

T cell activation leads to extensive clonal expansion, demanding a large amount of energy and biomass production (O'Neill et al., 2016; Olenchock et al., 2017). Glycolysis is central both in generating ATP and providing building blocks for macromolecular biosynthesis (Zhu and Thompson, 2019). Glycolysis catabolizes glucose into pyruvate through ten enzymatic reactions. In normoxic environments, pyruvate is typically transported into the mitochondria to be processed by the tricarboxylic acid cycle, driving OXPHOS for ATP production. In hypoxic environments, OXPHOS is suppressed and glycolysis is enhanced, generating lactate from pyruvate in order to regenerate nicotinamide adenine dinucleotide (NAD^+) needed to support ongoing glycolytic flux (Birsoy et al., 2015; Semenza, 2014; Sullivan et al., 2015). In highly proliferating cells, such as cancer cells and activated T cells, pyruvate can be converted into lactate in the presence of oxygen, a phenomenon termed aerobic glycolysis, or the "Warburg effect" (MacIver et al., 2013; Vander Heiden et al., 2009; Vander Heiden and DeBerardinis, 2017; Warburg et al., 1958; Zhu and Thompson, 2019). Although inhibiting glycolysis is an effective method of blocking T cell activation (Macintyre et al., 2014; Peng et al., 2016; Shi et al., 2011), inhibitors such as 2-Deoxy-D-glucose (2DG) have limited application in patients, due

87 to toxic side effects as a result of the housekeeping function of glycolysis in multiple cell types
88 (Raez et al., 2013).
89 Here, we systematically interrogate the requirement for individual glycolytic reactions in
90 Th17 cell models of inflammation and homeostatic function. We found that the glycolysis gene
91 *Gpi1* is unique in that it is selectively required by inflammatory pathogenic Th17 but not
92 homeostatic Th17 cells. All other tested glycolysis genes were essential for functions of both
93 Th17 cell types. Our mechanistic study revealed that upon Gpi1 loss during homeostasis, pentose
94 phosphate pathway (PPP) activity was sufficient to maintain basal glycolytic flux for biomass
95 generation, while increased mitochondrial respiration compensated for reduced glycolytic flux.
96 In contrast, Th17 cells in the inflammation models are confined to hypoxic environments and
97 hence were unable to increase respiration to compensate for reduced glycolytic flux. This
98 metabolic stress led to the selective elimination of Gpi1-deficient Th17 cells in inflammatory
99 settings but not in healthy intestinal lamina propria. Overall, our study reveals a context-
100 dependent metabolic requirement that can be targeted to eliminate pathogenic Th17 cells. As
101 Gpi1 blockade can be better tolerated than inhibition of other glycolysis components, it is a
102 potentially attractive target for clinical use.
103
104 **Results**
105
106 **Inflammatory Th17 cells have higher expression of glycolysis pathway genes than**
107 **commensal bacteria-induced homeostatic Th17 cells**
108 Commensal SFB induce the generation of homeostatic Th17 cells in the small intestine lamina
109 propria (SILP) (Ivanov et al., 2009), whereas immunization with myelin oligodendrocyte

110 glycoprotein peptide (MOG) in complete Freund's adjuvant (CFA) induces pathogenic Th17
111 cells in the spinal cord (SC), resulting in experimental autoimmune encephalomyelitis (EAE)
112 (Cua et al., 2003). Th17 cell pathogenicity requires expression of IL-23R (Ahern et al., 2010;
113 McGeachy et al., 2009). To identify genes involved in the pathogenic but not the homeostatic
114 Th17 cell program, we reconstituted Rag1$^{-/-}$ mice with isotype-marked *Il23r*-sufficient
115 (*Il23r*$^{GFP/+}$) and *Il23r* knockout (*Il23r*$^{GFP/GFP}$) bone marrow cells, and sorted CD4^{+} T cells of both
116 genetic backgrounds from the SILP of SFB-colonized mice and the SC of EAE mice for single
117 cell RNA sequencing (scRNAseq) analysis (Figure S1A). We identified 4 clusters of CD4^{+} T
118 cells in the SC of EAE mice and 5 clusters of CD4^{+} T cells in ileum lamina propria of SFB-
119 colonized mice (Figure S1B,C)). Clusters were annotated based on their signature genes, i.e.
120 Th17 cells (*Il17a*), Th1 cells (*Ifng*), Treg cells (*Foxp3*), and Tcf7^{+} cells (*Tcf7*) (Figure S1D,E).
121 Importantly, two of the EAE clusters consist mostly of IL-23R-sufficient T cells (Figures S1F-
122 H), indicating that these populations are likely pathogenic. One of them was annotated as Th17
123 and the other as Th1* according to earlier publications describing such cells as *Il23r*-dependent
124 IFN-γ producers (Hirota et al., 2011; Okada et al., 2015), and they were validated using flow
125 cytometry (Figure S1I). Importantly, pathway enrichment analysis revealed glycolysis as the top
126 pathway upregulated in both EAE Th17 and Th1* compared to the SFB-induced Th17 cells
127 (Figures S1J,K).
128 We selected a subset of genes that were differentially expressed in the pathogenic Th17/Th1*
129 cells (EAE model) versus the homeostatic Th17 cells (SFB model) for pilot functional studies
130 (Figures S1L,M). We developed a CRISPR- based T cell transfer EAE system to evaluate the
131 roles of the selected genes in pathogenicity (Figures S2A-C; see Methods). Among 12 genes
132 tested, only triosephosphate isomerase 1 (*Tpi1*), encoding an enzyme in the glycolysis pathway,

133 was required for disease onset following transfer of in vitro differentiated MOG-specific 2D2
134 TCR transgenic T cells (Figure S2D). This result was confirmed by analyzing *Tpi1*$^{f/f}$*Cd4*^{cre} mice,
135 which, unlike Tpi1$^{+/+}$ CD4^{cre} littermates, were completely resistant to EAE induction (Figure
136 1A). This finding prompted us to direct our focus on the glycolysis pathway. The relatively
137 sparse scRNAseq data detected the transcripts of only a few glycolysis pathway genes. We
138 therefore compared bulk RNAseq data of the two major pathogenic populations (Th1*: Klrc1^{+}
139 Foxp3^{RFP-}, Th17: IL17a^{GFP+} Klrc1^{-} Foxp3^{RFP-}) and the Treg cells (Foxp3^{RFP+} IL17a^{GFP-}) from the
140 spinal cord of EAE model mice and of the Th17 (IL17a^{GFP+} Foxp3^{RFP-}) and Treg (IL17a^{GFP-}
141 Foxp3^{RFP+}) cells from the SILP of the SFB model (Figures S2E, F). We found that almost every
142 glycolysis pathway gene was expressed at a higher level in the EAE model than in the SILP
143 CD4^{+} T cells, irrespective of whether cells were pathogenic or Treg (Figure 1B), suggesting that
144 most CD4^{+} T cells have more active glycoysis in the inflamed spinal cord microenvironment
145 than in the SILP at homeostasis.
146 Despite these differences in gene expression, Tpi1 was also indispensable for the SFB-
147 dependent induction of homeostatic Th17 cells. We analyzed CD4^{+} T cell profiles in chimeric
148 *Rag1* KO mice reconstituted with a 1:1 mix of bone marrow cells from *Tpi1*$^{+/+}$*CD4*^{cre} CD45.1/2
149 and *Tpi1*$^{f/f}$*CD4*^{cre} CD45.2/2 donors (Figure S3A). Tpi1 deficiency led to 33-fold reduction of
150 total CD4^{+} T cells in the SILP and to 1.4-fold and 1.7-fold reduction in the mLN and the
151 peripheral blood, respectively (Figure 1D). Moreover, RORγt, Foxp3, IL-17a, and IFN-γ were all
152 severely reduced in mutant T cells relative to the WT cells in the SILP and mLN (Figures
153 S3A,B). The same pattern was observed in the EAE model, using mixed bone marrow chimeric
154 mice (Figures 1E, and S3C), indicating that Tpi1 is essential for the differentiation of all CD4^{+} T
155 cell subsets.

156

157 **Gpi1 is selectively required by inflammatory but not homeostatic Th17 cells**

158 The higher glycolytic activity of the inflammatory Th17 cells suggested that they may be more
159 sensitive than the homeostatic Th17 cells to inhibition of glycolysis, which might be achieved by
160 inactivation of *Tpi1, Gpi1 or Ldha* (explained in figure S4A). However, neither cell type is likely
161 to survive a complete block in glycolysis by *Gapdh* knockout. To test the hypothesis, we
162 assessed the ability of co-tranferred control and targeted TCR transgenic T cells to differentiate
163 into Th17 cells in models of homeostasis (7B8 T cells in SFB-colonized mice (Yang et al.,
164 2014)) and inflammatory disease (2D2 T cells for EAE (Bettelli et al., 2003) and HH7.2 T cells
165 for *Helicobacter*-dependent transfer colitis (Xu et al., 2018)) (Figure 2A). The genes of interest
166 (indicated in Figure S4A) or the control gene *Olfr2* were inactivated by guide RNA
167 electroporation of naïve isotype-marked $CD4^+$ TCR and Cas9 transgenic T cells (Platt et al.,
168 2014), which were then transferred in equal numbers into recipient mice (Figures 2A, S4B).
169 Targeting was performed with sgRNAs that achieved the highest in vitro knockout efficiency
170 (~80-90%) (Figures S4C-E), which corresponded to the frequency of targeted cells at 4 days
171 after electroporation and transfer into mice, as assessed by targeting of GFP (Figure S4B). This
172 strategy also allowed for efficient double gene KO (Figure S4F).

173 In both SFB and EAE T cell transfer experiments, there were roughly 9-fold fewer *Tpi1*-
174 targeted than co-transferred control Th17 cells in the SILP or the SC, respectively (Figures 2B-
175 D), consistent with the *in vitro* KO efficiency (Figure S4C), suggesting that the majority of the
176 *Tpi1* KO cells were eliminated in the total T cell pool. The remaining cells expressed RORγt and
177 IL-17a at a similar level to control populations (Figures S5A-D), which was not observed in the
178 previous *Tpi1* bone marrow-reconstituted mice (Figures S3B), suggesting that they were not

179 targeted. These results indicated that the electroporation transfer system could be successfully
180 used to evaluate T cell gene functions *in vivo*.
181 Similar to the *Tpi1* KO, cells deficient for *Gapdh* were eliminated in all three models tested
182 (Figures 2B-E). Inactivation of *Ldha* resulted in loss of the cells in the EAE model, and a less
183 striking, but still substantial, cell number reduction in the homeostatic SFB model (Figures 2B-
184 E). In contrast, although *Gpi1* ablation reduced cell number by 75% in the inflammatory EAE
185 and colitis models, it had no significant effect on cell number in the homeostatic Th17 cell model
186 (Figures 2B-E). Consistent with the reduction in cell number, *Gpi1*-mutant 2D2 cells were
187 unable to induce EAE (Figure 2F), suggesting that Gpi1 is essential for pathogenicity. We also
188 investigated Th17 cell differentiation and cytokine production by *Gpi1*-deficient cells in the SFB
189 model, and found no difference from co-transferred control cells in terms of RORγt/Foxp3
190 expression (Figures 2G) or IL-17a production, as demonstrated using 7B8 cells from mice bred
191 to the *Il17a*$^{GFP/+}$ reporter strain (Figure 2H). *In vitro* restimulation further confirmed that
192 transferred Gpi1-targeted 7B8 cells were indeed Gpi1 deficient (Figures S5C, D). Collectively,
193 these data suggest that Gpi1 is selectively required by the inflammatory encephalitogenic and
194 colitogenic Th17 cells, but not by homeostatic SFB-induced Th17 cells. In contrast, Gapdh,
195 Tpi1 and Ldha are required for the accumulation of both types of Th17 cells.
196
197 **PPP compensates for Gpi1 deficiency in the homeostatic SFB model**
198 To explain why Gpi1 is dispensable in the homeostatic SFB model while other glycolysis genes
199 are not, we hypothesized that the PPP shunt might maintain some glycolytic activity in the *Gpi1*
200 KO cells and thus compensate for Gpi1 deficiency (Figure S4A). We tested the hypothesis with
201 *in vitro* isotope tracing. Irrespective of the non-pathogenic (npTh17, cultured in IL-6 and TGF-

202 β (Veldhoen et al., 2006)) or pathogenic (pTh17, cultured in IL-6, IL-1β, and IL-23 (Ghoreschi
203 et al., 2010)) conditions used, *in vitro* differentiated Th17 cells displayed less of a growth defect
204 (25% reduction) following targeting of *Gpi1* than upon inactivation of *Gapdh* (70% reduction)
205 (Figure 3A). This result resembles the different sensitivities observed in the homeostatic SFB
206 model, suggesting that the cytokine milieu of the pathogenic and homeostatic Th17 cells does
207 not account for the phenotypes of the *Gpi1* mutant mice. We incubated np/p Th17 cells with
208 $^{13}C_{1,2}$-glucose and analyzed downstream ^{13}C label incorporation. The $^{13}C_{1,2}$-glucose tracer is
209 catabolized through glycolysis via Gpi1, producing pyruvate or lactate containing two heavy
210 carbons (M2), while Gpi1-independent shunting through the PPP produces pyruvate and lactate
211 containing one heavy carbon (M1) (Figure 3B) (Lee et al., 1998). Consistent with our hypothesis,
212 we observed ~ 3-fold increase in relative PPP activity in the *Gpi1* KO Th17 cells compared to
213 the *Olfr2* KO control, irrespective of npTh17 or pTh17 condition (Figure 3C), indicating that
214 *Gpi1* deficiency maintains active glycolytic flux through PPP shunting.
215 To test whether PPP activity compensates for Gpi1 deficiency *in vivo* in the homeostatic SFB
216 model, we knocked out both *Gpi1* and *G6pdx*, which catalyzes the initial oxidative step in the
217 PPP, with the CRISPR-electroporation transfer system. Combined deletion of these two genes
218 would be expected to block glycolysis, similar to *Gapdh* KO. Consistent with this hypothesis, the
219 *Gpi1/G6pdx* double KO reduced cell number by about 75%, which is similar to that with the
220 *Gapdh* single KO, yet significantly different from that with inactivation of either *Gpi1* or *G6pdx*
221 alone (Figure 3D). These results suggest that *in vivo* PPP activity maintains viability of the
222 homeostatic SFB-induced Th17 cells lacking Gpi1.
223

224 **Increased mitochondrial respiration additionally compensates for Gpi1 deficiency in the**
225 **homeostatic SFB model**
226 To determine the impact of Gpi1 deficiency on aerobic glycolysis activity, we quantified lactate
227 production by GC-MS and found it to be markedly reduced in *Gpi1* KO cells (Figure 4A). A
228 significant reduction in lactate production may suggest compromised glycolytic ATP production
229 in *Gpi1* KO cells. As *in vitro* cultured *Gpi1* KO Th17 cells and homeostatic SFB-specific *Gpi1*
230 KO Th17 cells were largely unaffected in terms of cell number and cytokine production, we
231 speculate that mitochondrial respiration may provide an alternative source of ATP to
232 compensate. Indeed, in vitro cultured *Gpi1* KO cells displayed higher ATP-linked respiration
233 rate than *Olfr2* control cells, irrespective of npTh17 or pTh17 cell culture condition (Figure
234 4B,C). Furthermore, upon Antimycin A (Complex III inhibitor) treatment, *Gpi1* KO cells were
235 decreased in cell number, similar to *Gapdh*-deficient cells (Figure 4D), consistent with increased
236 mitochondrial respiration compensating for Gpi1 deficiency in the *in vitro* cell culture system.
237 To determine whether increased respiration rescues Gpi1 deficiency *in vivo* in the
238 homeostatic SFB model, we targeted *Gpi1* in 7B8 T cells along with genes responsible for the
239 oxidation of three major substrates feeding the TCA cycle: *Pdha1* (pyruvate), *Gls1* (glutamine),
240 and *Hadhb* (fatty acids). Following co-transfer of control cells and cells lacking either *Pdha1*,
241 *Gls1*, or *Hadhb*, there was no defect in Th17 cell number, RORγt expression, or cytokine
242 production (data not shown). However, only double knockout of *Gpi1* and *Pdha1* led to a
243 significant reduction in cell number, similar to that with the *Gapdh* KO cells (Figure 4E),
244 suggesting that mitochondrial respiration through pyruvate oxidation compensates for Gpi1
245 deficiency in homeostatic Th17 cell differentiation induced by SFB colonization.
246

247 **PPP utilization favors biosynthetic metabolite synthesis in Gpi1-deficient cells**

248 Compensation for *Gpi1* deletion by the combination of the PPP and mitochondrial respiration
249 suggests the existence of a partial metabolic redundancy for Gpi1. To understand the
250 compensatory mechanism, we performed kinetic flux profiling, employing GC-MS to measure
251 the passage of isotope label from $^{13}C_6$-glucose into downstream metabolites (Yuan et al., 2008).
252 The resulting kinetic data, along with metabolite abundance, was used to quantify metabolic flux
253 in npTh17 cells prepared from *Gpi1* KO, *Olfr2* KO and cells treated with koningic acid (KA), to
254 inhibit Gapdh (Liberti et al., 2017), since more than 50% of cells in the *Gapdh* KO culture were
255 WT escapees (Figure S4C)).

256 Loss of Gpi1 resulted in reduction of glucose uptake (Figure 5A) and in substantially
257 decreased transmission of isotopic label to intracellular pyruvate and lactate, whose abundance
258 was also reduced (Figures 5C,D,I). Interestingly, a lower lactate production/glucose
259 consumption ratio was observed in *Gpi1* KO than control cells (Figure 5B), suggesting that
260 Gpi1-deficient cells may be more inclined to use glucose carbons for the synthesis of
261 biosynthetic metabolites, rather than lactate production. Indeed, the labeling rate and total
262 abundance of the biosynthetic metabolites alanine, serine, glycine, and citrate either did not
263 change or were slightly increased in the *Gpi1* KO cells (Figures 5E-I). The flux of pyruvate,
264 lactate, alanine, serine, and glycine in the Gpi1-deficient cells, as compared to *Olfr2* KO control
265 (Figure 5J), was consistent with the PPP supporting the branching pathways of glycolysis
266 important for biosynthetic metabolite production, despite a reduced glycolysis rate. In contrast,
267 Gapdh inhibition by KA treatment almost completely prevented the synthesis of downstream
268 metabolites (Figures 5C-H) and lactate production (Figure 5K). However, it did not induce an
269 increase in OCR (Figures 5K, L), possibly due to the severely limited production of pyruvate.

270 Taken together, we conclude that the reduced amount of glucose metabolized via the PPP by
271 *Gpi1*-deficient cells was sufficient to support the production of glycolytic intermediates and
272 maintain pyruvate oxidation. *Gpi1*-deficient cells increased their mitochondrial respiration to
273 compensate for the loss of glycolytic flux. In contrast, glycolytic blockade by Gapdh inhibition
274 completely prevented carbon flux needed for key biosynthetic metabolites, which is incompatible
275 with cell viability.
276
277 **Gpi1 is essential in the hypoxic setting of Th17-mediated inflammation**
278 To understand why inflammatory Th17 cells are particularly sensitive to Gpi1 deficiency, we
279 reasoned that metabolic compensation (either through PPP or mitochondrial respiration), which
280 occurs in the homeostatic model, may be restricted in inflammatory Th17 cells. *G6pdx* KO in the
281 EAE model resulted in a 70% reduction in 2D2 cell number in the spinal cord (Figures S6A,B),
282 suggesting that PPP flux is still active in the setting of inflammation. On the other hand, a
283 number of reports have shown that inflamed tissues, including the spinal cord in EAE and the
284 LILP in colitis, are associated with low oxygenation (hypoxia) (Davies et al., 2013; Johnson et
285 al., 2016; Karhausen et al., 2004; Naughton et al., 1993; Ng et al., 2010; Peters et al., 2004; Van
286 Welden et al., 2017; Yang and Dunn, 2015). This suggests that impaired mitochondrial
287 respiration might occur which would result in an inability to provide sufficient ATP to
288 compensate for energy loss due to Gpi1 deficiency in these tissues. To test this hypothesis, we
289 cultured Th17 cells in normoxic (20% O_2) and mild hypoxic (3% O_2) conditions, and found that
290 *Gpi1* KO Th17 cells in the hypoxic state, irrespective of npTh17 or pTh17 differentiation
291 protocols, displayed a growth defect similar to that occurring with Gapdh deficiency (Figure
292 6A). Furthermore, Olfr2 control npTh17 cells displayed about a 2-fold increase in lactate

293 production in hypoxic compared to normoxic conditions (Figure S6C), indicating that hypoxic
294 cells rely more on glycolysis to generate ATP. *Gpi1* KO cells had substantially decreased lactate
295 production in both normoxic and hypoxic conditions (Figure S6C), but there was reduced
296 intracellular ATP only with hypoxia (Figure S6D), suggesting that restrained mitochondrial
297 respiration in hypoxia cannot compensate for Gpi1 inactivation, and hence leads to energy crisis.
298 We next investigated whether the inflamed tissue in the EAE model differs from the
299 homeostatic tissue in the SFB model with regard to oxygen availability. To address this, we
300 performed I.V. injection of pimonidazole, an indicator of O_2 levels, into mice with EAE or with
301 SFB colonization, and found that $CD4^+$ T cells in the EAE model spinal cord had two-fold
302 higher pimonidazole staining than in the dLN and ~2.7-fold compared to $CD4^+$ T cells in SILP
303 and mLN (Figure 6B). This result suggests that $CD4^+$ T cells in the spinal cord of the EAE
304 model experience greater oxygen deprivation than in other tissues examined. The increased
305 labeling in the spinal cord was observed in all subsets of $CD4^+$ T cells (Figures S6E,F),
306 indicating that decreased oxygen availability is likely a tissue feature.
307 Hif1α is an oxygen sensor that, upon activation by hypoxia, initiates transcription of genes,
308 including glycolysis genes, to allow cells to adapt in poorly oxygenated tissue (Corcoran and
309 O'Neill, 2016; Lee et al., 2020; Semenza, 2013). To further examine the oxygenation level of
310 SILP and SC, we investigated the effect of *Hif1a* deficiency in the different models of $CD4^+$ T
311 cell differentiation. Using chimeric *Rag1* KO mice reconstituted with equal numbers of
312 *Hif1a*$^{+/+}$*CD4*^{cre} and *Hif1a*$^{f/f}$*CD4*^{cre} bone marrow cells, there was ~ 40% reduction of Hif1α-
313 deficient $CD4^+$ T cells in the spinal cord of mice with EAE, but little difference in the SILP
314 (Figures 6C-E). Furthermore, in the SILP of SFB-colonized mice, there was no significant
315 difference in RORγt and Foxp3 expression or IL-17a and IFN-γ production between WT and KO

316 $CD4^+$ T cells (Figures S6G,H). In contrast, in the spinal cord of the EAE mice, there was a slight
317 decrease in the Th17 cell fractions and increase in the $Foxp3^+$ fraction in the *Hif1a* KO compared
318 to WT $CD4^+$ T cells (Figures S6G, H). Overall, these data suggest that Hif1α is functionally
319 important for the pathogenic Th17 cells (as well as Treg cells) in the EAE model, but not for
320 homeostatic SILP Th17 cells, reinforcing the conclusion of the pimonidazole experiment that T
321 cells in the inflamed spinal cord experience greater oxygen deprivation than those in the healthy
322 small intestine lamina propria.

323 To address when and how Gpi1 deficiency impairs inflammatory Th17 cell differentiation
324 and/or function, we performed a time course experiment to assess the kinetics of the co-
325 transferred *Olfr2* KO control and *Gpi1* KO 2D2 cells in the EAE model. *Gpi1* KO T cells, like
326 *Olfr2* KO control cells, were maintained in the dLN until day 13, the last time point when
327 transferred 2D2 cells were still detectable in the dLN (Figure 6E). However, at 13 days post
328 immunization, *Gpi1* mutant cell number was reduced by 50% compared to control T cells in the
329 spinal cord (Figure 6E). This finding is consistent with the previous observation that the spinal
330 cord, but not the dLN, is hypoxic. Accordingly, we observed reduced proliferation of *Gpi1* KO
331 2D2 cells in the spinal cord but not in the dLN (Figures 6F and S6I). Importantly, 2D2 cells in
332 the dLN of mice with EAE proliferated at a markedly faster rate than 7B8 cells in the mLN of
333 the SFB model (Figures S6J,K). This demonstrates that Gpi1-deficient 2D2 cells can maintain
334 the higher demand for energy and biomass associated with rapid proliferation and emphasizes
335 the role of the SC hypoxic environment in the T cell's dependence on Gpi1. We also examined
336 Th17 cell differentiation/cytokine production, by staining for RORγt/Foxp3 and IL-17a,
337 apoptosis, by staining for the active form of caspase 3, and potential for migration, by staining
338 for Ccr6, and observed no differences between *Gpi1*-deficient and co-transferred control *Olfr2*

339 KO 2D2 T cells (Figures S6L-P). We conclude that Th17 cells increase glycolysis activity to
340 adapt to the hypoxic environment in the EAE spinal cord, and the restrained mitochondrial
341 respiration in this setting cannot compensate for the loss of glycolytic ATP production upon
342 Gpi1 inactivation, leading to energy crisis and cell elimination.
343
344 **Discussion**
345
346 Our results demonstrate the remarkable plasticity of cellular metabolism owing to redundant
347 components in the network, and highlight that plasticity can vary based on microenvironmental
348 factors. Due to the unique position of Gpi1 in the glycolysis pathway, its deficiency was
349 compensated by the combination of two metabolic pathways – the PPP and mitochondrial
350 respiration. The PPP maintained glycolytic activity, albeit at a reduced level, to fully support
351 biosynthetic precursor synthesis through branching pathways. Pyruvate, which is also produced
352 by way of the PPP, increased its flux into the TCA cycle, elevating ATP production from
353 mitochondrial respiration, thus compensating for loss of ATP production from glycolysis.
354 Therefore, upon Gpi1 inactivation, homeostatic SFB-induced Th17 cells reprogrammed their
355 metabolism, retaining the ability to provide adequate biomass and energy to support cell
356 function. In contrast, limitation of mitochondrial respiration due to low oxygen availability in the
357 inflamed EAE spinal cord rendered Gpi1-deficient cells unable to generate sufficient ATP
358 molecules either through glycolysis or mitochondrial respiration, resulting in energy crisis and
359 cell elimination. Inactivation of Gapdh, whose function, unlike that of Gpi1, cannot be
360 compensated by other metabolic pathways, completely blocked glycolysis and hence led to
361 elimination of both homeostatic and inflammatory Th17 cells. Our results suggest not only that

362 suppressing glycolysis by Gpi1 inhibition could be a well-tolerated treatment for hypoxia-related
363 autoimmune diseases, but also that metabolic redundancies can be exploited for targeting disease
364 processes in selected tissues.
365
366 **Metabolic requirements for CD4$^+$ T cell activation and differentiation**
367 We found that CD4$^+$ T cells (pathogenic or Treg) in the EAE model had greater expression of
368 glycolytic genes than homeostatic CD4$^+$ T cells, which is consistent with the recent
369 demonstration that *Citrobacter*-induced inflammatory Th17 cells were more glycolytic than
370 SFB-induced homeostatic Th17 cells (Omenetti et al., 2019). Our data suggest that T cells adapt
371 to the hypoxic environment in the inflamed spinal cord by up-regulating glycolysis, most likely
372 by hypoxia-stabilized Hif1α.
373 In spite of the difference in glycolytic activity, blockade of glycolysis by *Gapdh* KO is
374 incompatible with Th17 cell expansion and differentiation in either homeostatic or inflammatory
375 models. However, the finding that Gpi1-deficient 2D2 T cells proliferated normally in the dLN
376 of the EAE model suggests that T cell activation and differentiation *in vivo* do not necessarily
377 need a fully functional glycolytic pathway. With the PPP providing sufficient metabolites for
378 biomass production and mitochondria generating greater amounts of ATP, T cell proliferation
379 and execution of the non-pathogenic Th17 program *in vivo* can be largely maintained in the *Gpi1*
380 KO cells. Our data highlight the complexity of the glycolysis pathway and suggest that not every
381 enzyme is equally important to glycolytic activity and cell function.
382 Treg cell differentiation has been proposed to depend on OXPHOS (Kullberg et al., 2006;
383 Macintyre et al., 2014; MacIver et al., 2013; Michalek et al., 2011), and was promoted by
384 glycolysis inhibition *in vitro* with 2DG (Shi et al., 2011). Our *in vivo* genetic data however

385 support an indispensable role of glycolysis in Treg cell differentiation, as demonstrated by
386 complete loss of the intestinal and SC Foxp3$^+$ T cells in mice deficient for *Tpi1* in T cells.
387 One intriguing finding that we have not characterized in detail is the dispensable role of
388 Pdha1, Gls1, and Hadhb in SFB-induced homeostatic Th17 cell differentiation. While OXPHOS
389 is essential for SFB-specific Th17 cells (data not shown), their ability to differentiate in the
390 absence of genes controlling metabolite fueling of the TCA cycle suggests potential
391 redundancies. Furthermore, the discrepancy between the in vivo and in vitro function of
392 Pdha1(as shown in this study) and Gls1 (by comparing the in vivo data in this study with
393 reported in vitro data (Johnson et al., 2018)) suggests that the microenvironment is critical for T
394 cell metabolism and gene function, as does a recent report showing distinct metabolism profiles
395 of in vivo and in vitro activated T cells (Ma et al., 2019).
396
397 **Gpi1 as a drug target for hypoxia-related diseases**
398 Our study reveals that Gpi1 may be a good drug target for Th17-mediated autoimmune diseases.
399 The sensitivity to Gpi1 deficiency is dependent on whether cells are competent to increase
400 mitochondrial respiration. Therefore, other disease processes involving hypoxia-related
401 pathologies may also be susceptible to Gpi1 inhibition. A recent report showed that 1% O_2
402 almost completely inhibited *in vitro* growth of *Gpi1*-mutant tumor cell lines, but the proliferation
403 defect was much milder when cells were cultured in normoxic condition (de Padua et al., 2017).
404 This suggests that hypoxia-mediated sensitivity to Gpi1 deficiency can be a general
405 phenomenon, from Th17 cells to tumor cells, which may extend the deployment of Gpi1
406 inhibition to a broader range of diseases.

407 Sensitivity to inhibition of both Hif1α and Gpi1 is dependent on oxygen availability. In the
408 mixed bone marrow chimera experiments with the EAE model, there was less than a 2-fold
409 reduction in *Hif1a* mutant compared to wild-type spinal cord $CD4^+$ T cells, whereas *Gpi1*-
410 targeted T cells were reduced 5-fold compared to wild-type cells in the transfer model of EAE.
411 *Hif1a* inactivation efficiency was almost complete (data not shown), while *Gpi1* KO efficiency
412 was roughly 80%, which suggests that Gpi1 deficiency resulted in a more severe defect than
413 *Hif1a* deficiency when the T cells were in a hypoxic environment. This is not unexpected, as
414 Gpi1 itself participates in the glycolysis pathway while Hif1α regulates the transcription of genes
415 in the pathway. Although EAE was attenuated following *Hif1a* inactivation in $CD4^+$ T cells
416 (Dang et al., 2011; Shi et al., 2011), our results suggest that Gpi1 inhibition may be at least as
417 effective a means of blocking cell function in hypoxic microenvironments.
418 While our data suggest that hypoxia is an essential factor that restains proliferation of Gpi1-
419 deficient Th17 cells in the spinal cord, we cannot exclude the possibility that other
420 environmental factors also contribute to the phenotype, as oxygenation level is certainly not the
421 only difference between the inflamed spinal cord and the healthy small intestine lamina propria.
422

423 **Gpi1 targeting can be tolerated**

424 Glycolysis is a universal metabolic pathway whose blockade by inhibitors such as 2DG can yield
425 adverse side effects even at dosages too low to control tumor growth (Raez et al., 2013). 2DG
426 inhibits the first three steps of glycolysis, an effect that is recapitulated by Gapdh inhibition,
427 given that no alternative pathway exists for glucose catabolism. Although glycolysis is essential
428 for T cell activation, treating diseases caused by autoimmune T cells with drugs that fully inhibit
429 the pathway, e.g. 2DG or KA, would also likely be too toxic at potentially efficacious dosages.

430 In light of the results presented here, Gpi1 may represent a better drug target than other
431 glycolysis gene products for treating Th17 cell-mediated autoimmune diseases, as targeting Gpi1
432 may be well tolerated by most cells and tissues, thus causing minimal side effects.
433 This hypothesis is supported by genetic data obtained from patients with glycolysis gene
434 deficiencies. With few exceptions, patients deficient for *Tpi1* or *Pgk1* have combined symptoms
435 of anemia, mental retardation and muscle weakness [Online Mendelian Inheritance in Man
436 (OMIM) entry 190450, 311800] (Schneider, 2000). Mutations in glycolysis gene products that
437 have redundant isozymes can result in dysfunction of cell types in which only the mutated
438 isozyme gets expressed, such that *Pgam2* deficiency results in muscle breakdown and *Pklr*
439 deficiency causes anemia (Zanella et al., 2005). The human genetic data are thus consistent with
440 the prediction that inhibition of glycolysis enzymes would result in serious side effects.
441 However, the vast majority of patients with *Gpi1* mutations, which can result in preservation of
442 less than 20% enzymatic activity, have mild to severe anemia that is treatable, with no
443 neurological or muscle developmental defects (Baronciani et al., 1996; Kanno et al., 1996;
444 Kugler et al., 1998; McMullin, 1999; Zaidi et al., 2017) [OMIM entry 172400]. These clinical
445 data indicate that neurons and muscle cells can afford losing most of their Gpi1 activity even
446 though they require glycolysis, and hence they behave similarly to homeostatic Th17 cells.
447 Collectively, these patient data strongly support our proposal that Gpi1 can be a therapeutic
448 target.
449
450 **Selective metabolic redundancies permit selective cell inhibition**
451 Metabolic redundancy has been demonstrated in many biological systems, from bacteria to
452 cancer cell lines (Bulcha et al., 2019; Deutscher et al., 2006; Horlbeck et al., 2018; Segre et al.,

453 2005; Thiele et al., 2005; Zhao et al., 2018). Our study demonstrates compensatory metabolic
454 pathways in $CD4^+$ T cells *in vivo*, and highlights that such redundancy can be selective,
455 depending on the cellular microenvironment. Indeed, specific inhibition of pathogenic cells can
456 be achieved by metabolic targeting of selective redundant components. Therefore,
457 characterization of the metabolic redundancy of cells in microenvironments with varying oxygen
458 level, pH, abundance of extracellular metabolites, redox status, cytokine milieu, or temperature,
459 may provide opportunities for metabolic targeting of cells in selected tissue microenvironments
460 for therapeutic purposes.
461
462 **Acknowledgements:** We thank the NYU Langone Genome Technology Center for expert
463 library preparation and sequencing. This shared resource is partially supported by the Cancer
464 Center Support Grant P30CA016087 at the Laura and Isaac Perlmutter Cancer Center. We thank
465 Drew R. Jones and Rebecca E. Rose in the NYU Metabolomics Laboratory for helpful
466 discussion and aid with LC-MS data generation and analysis. We thank S.Y. Kim in the NYU
467 Rodent Genetic Engineering Laboratory (RGEL) for generating the Tpi1 conditional KO mice.
468 We thank Anne R. Bresnick (Department of Biochemistry, Albert Einstein College of Medicine)
469 for sharing the S100a4 mutant mice. This work was supported by National Multiple Sclerosis
470 Society Fellowship FG 2089-A-1 (L.W.), by Immunology and Inflammation training grant
471 T32AI100853 (C.N.), by NIH grant R01AI121436 (D.R.L.), by the Howard Hughes Medical
472 Institute (D.R.L.), and the Helen and Martin Kimmel Center for Biology and Medicine (D.R.L.)
473
474 **Author Contributions:** L.W. and D.R.L. conceived the project, and wrote the manuscript. L.W.
475 designed, performed experiments, and analyzed the data. L.W. and K.E.R.H. designed,

476 performed the GC-MS flux, tracing, and seahorse experiments, analyzed the data. Y.H. and R.S.
477 analyzed the scRNAseq data. L.K. analyzed the bulk RNAseq data. C.A., W.L., D.L., and
478 H.M.S. helped with mouse experiments. C.N. and W.L. helped with the development of the
479 CRISPR/Cas9 transfection method. S.J. and R.P. helped with GC-MS experiments. K.E.R.H.,
480 J.J.L., R.P., M.E.P., T.Y.P., and A.C.K. assisted with the analysis and interpretation of the
481 metabolic data. K.E.R.H., H.M.S., S.J., J.J.L., R.P., M.E.P., T.Y.P., A.C.K., and R.S. edited the
482 manuscript. D.R.L. supervised the work.
483
484 **Declaration of Interests:** D.R.L. consults and has equity interest in Chemocentryx, Vedanta,
485 and Pfizer Pharmaceuticals. The NYU School of Medicine has filed a provisional patent
486 application related to this work.
487
488 **Main figure titles and legends**
489 **Figure 1. Encephalitogenic Th17 cells have higher glycolysis pathway gene expression than**
490 **homeostatic SFB-induced Th17 cells.**
491 (A) Clinical disease course of MOG-CFA-induced EAE in *Tpi1*$^{f/f}$*Cd4*^{cre} (n=7) and *Tpi1*$^{+/+}$*Cd4*^{cre}
492 littermate control mice (n=8). The experiment was repeated twice with the same
493 conclusion. P values were determined using two-way ANOVA, * (P<0.05), ****
494 (P<0.0001).
495 (B) Heatmap of glycolysis pathway genes expressed in spinal cord Th1*, Th17, and Treg cells in
496 mice with EAE (day 15, score 5) compared to Th17 and Treg cells in the SILP of SFB-
497 colonized mice. Genes are arranged according to the fold change between EAE Th17 and
498 SFB Th17.

499 (C) Experimental design of the Tpi1 bone marrow reconstitution experiment. Bone marrow cells
500 from *Tpi1*$^{+/+}$ *Cd4*^{cre} CD45.1/2 and *Tpi1*$^{f/f}$ *Cd4*^{cre} CD45.2/2 donor mice were transferred into
501 lethally irradiated CD45.1/1 recipients. Peripheral blood was collected two months later for
502 reconstitution analysis. dLN and SC of the EAE model, and mLN and SILP of the SFB
503 model were dissected at day 15 post EAE induction or SFB colonization.
504 (D,E) Cell number analysis of *Tpi1* WT and KO CD4^{+} T cells in the SFB model (D) and the
505 EAE model (E). Left panels, representative FACS plots showing the frequencies of the
506 CD45.1/2 and the CD45.2/2 B cells among all B cells in peripheral blood and of the
507 CD45.1/2 and the CD45.2/2 CD4^{+} T cells among all CD4^{+} T cells in peripheral blood, mLN
508 or dLN, and SILP of SFB colonized mice or SC of EAE mice. Middle panels, compilation of
509 the cell number ratio of CD45.2/2 to CD45.1/2. Right, normalized KO/WT total CD4^{+} T cell
510 number ratio in each tissue. The cell number ratio of peripheral B cells was set as 1. P values
511 were determined using paired t tests.
512 See also Figures S1,2,3.
513
514 **Figure 2. Gpi1 is selectively required by inflammatory encephalitogenic or colitogenic Th17**
515 **cells, but not by homeostatic SFB-induced Th17 cells.**
516 (A) Experimental setup. TCR transgenic Cas9-expressing naïve CD4^{+} T cells were electroporated
517 with guide amplicons, and co-transferred with *Olfr2* amplicon-electroporated control cells
518 into recipient mice that were immunized for EAE induction (EAE model), or had been
519 colonized with SFB (SFB model) or *Helicobacter hepaticus* (Colitis model).
520 (B) Representative FACS plots showing the frequencies of *Olfr2* KO cells and the co-transferred
521 glycolytic gene KO cells among total CD4^{+} T cells in each model.

522 (C-E) Compilation of cell number ratio of gene KO group to the co-transferred *Olfr2* control for
523 each model, as shown in panel B. The ratio was normalized to *Olfr2*/*Olfr2* co-transfer
524 (*Olfr2*/*Olfr2* cell number ratio was set to 1). Three independent experiments were performed
525 with the same conclusion.
526 (F) Clinical disease course of EAE in *Rag1* KO mice receiving *Olfr2* KO 2D2 cells or *Gpi1* KO
527 2D2 cells. Experiment was conducted as illustrated in Figure S2C. n=5 mice/group. The
528 experiment was repeated twice with the same conclusion.
529 (G) Left, representative FACS plot showing RORγt and Foxp3 expression of co-transferred
530 targeted 7B8 cells isolated from the SILP of recipient SFB-colonized mice at day15. Right,
531 ratio of the percentage of RORγt^{+} Foxp3^{-} in *Gpi1*- or *Olfr2*-targeted versus co-transferred
532 *Olfr2* control cells in each recipient.
533 (H) Left, representative FACS histogram showing the overlay of IL17a-GFP expression of co-
534 transferred *Olfr2* KO and *Gpi1* KO 7B8 cells isolated from the SILP of SFB-colonized mice
535 at day15. Right, ratio of the percentage of IL-17a^{+} cells in *Gpi1*- or *Olfr2*-targeted versus co-
536 transferred *Olfr2* control cells in each recipient.
537 P values were determined using t tests.
538 See also Figures S4,5.
539
540 **Figure 3. PPP activity rescues *Gpi1* deficiency in the homeostatic SFB-induced Th17 cells**
541 (A) Relative number of Th17 cells cultured for 120 h *in vitro*. Naïve Cas9-expressing CD4^{+} T
542 cells were electroporated with corresponding guide-amplicons and cultured in both npTh17
543 condition and pTh17 condition. Cell number was normalized to *Olfr2* KO group (*Olfr2* cell
544 number was set as 100). N=3, data are representative of three independent experiments.

545 (B) Schematic of $^{13}C_{1,2}$-glucose labeling into downstream metabolites. ^{13}C is labeled as filled
546 circle. Catalytic reactions of PPP are labeled as red arrows, while those of glycolysis are in
547 black.
548 (C) Relative PPP activity of *in vitro* cultured Th17 cells. Relative PPP activity from $^{13}C_{1,2}$-
549 glucose was determined using the following equation: PPP= M1/ (M1+M2), where M1 is the
550 fraction of $^{13}C_{1,2}$-glucose derived from the PPP and M2 is the fraction of $^{13}C_{1,2}$-glucose
551 derived from glycolysis.
552 (D) 7B8 Cas9 transgenic naïve $CD4^+$ T cells were electroporated with a mixture of two guide
553 amplicons (for double KO) before being transferred into recipient mice. Left, representative
554 FACS plots showing the frequencies of co-transferred *Olfr2*+*Olfr2* control $CD4^+$ T cells and
555 the indicated gene KO $CD4^+$ T cells in the SILP of the SFB model. Right, compilation of cell
556 number ratios of the indicated gene KO combinations to the co-transferred *Olfr2*+*Olfr2*
557 control. The ratio was normalized to *Olfr2*+*Olfr2*/*Olfr2*+*Olfr2* co-transfer. Two independent
558 experiments were performed with same conclusion.
559 P values were determined using t tests.
560
561 **Figure 4. Mitochondrial respiration compensates for Gpi1 deficiency in the homeostatic**
562 **SFB Th17 cells**
563 (A) Lactate secretion of *in vitro* cultured *Olfr2* and *Gpi1* KO np/p Th17 cells. Cells were cultured
564 as in Figure 3A. At 96 h cells were re-plated in fresh RPMI medium with 10% dialyzed FCS,
565 and supernatants were collected 12 h later for lactate quantification by GC-MS.
566 (B) Seahorse experiment showing the oxygen consumption rate (OCR) of *in vitro* cultured Th17
567 cells at baseline and in response to oligomycin (Oligo), carbonyl cyanide 4-

568 (trifluoromethoxy) phenylhydrazone (FCCP), and rotenone plus antimycin (R + A). 10
569 replicates were used for the npTh17 *Olfr2* and *Gpi1* targeted cells, 7 replicates for the pTh17
570 *Olfr2*, and 6 replicates for the pTh17 *Gpi1* sets of targeted cells.
571 (C) ATP linked respiration rate quantified based on experiments in panel (B). Representative
572 data from three independent experiments.
573 (D) Relative number of Th17 cells cultured for 120 h *in vitro* (as in Figure 3A), in the presence or
574 absence of 10 nM antimycin A. Cell number was normalized to control (*Olfr2*-targeted cell
575 number was set as 100). n=3, data are representative of two independent experiments.
576 (E) 7B8 Cas9 naïve $CD4^+$ T cells were electroporated with a mixture of two guide amplicons (for
577 double KO) before transfer into recipient mice. Left, representative FACS plots showing the
578 frequencies of co-transferred *Olfr2*+*Olfr2* control and indicated gene KO $CD4^+$ T cells in the
579 SILP of the SFB model at day 15. Right, compilation of cell number ratios of glycolysis gene
580 KO group to the co-transferred *Olfr2*+*Olfr2* control. The ratio was normalized to
581 *Olfr2*+*Olfr2*/*Olfr2*+*Olfr2* co-transfer. Three independent experiments were performed with
582 same conclusion.
583 P values were determined using t tests.
584
585 **Figure 5. PPP supports normal biomass synthesis in the *Gpi1*-deficient npTh17 cells**
586 *Olfr2*- or *Gpi1*-targeted npTh17 cells (cultured for 96 h as in Figure 3A) were collected for
587 further metabolic analysis.
588 (A, B) Cells were re-plated in U-$^{13}C_6$-glucose tracing medium to measure (A) glucose
589 consumption rate, and (B) ratio of released lactate to consumed glucose by LC-MS.

590 (C-H) Cells were re-plated in U-$^{13}C_6$-glucose tracing medium, and cell pellets were collected at
591 different time points to measure ^{13}C incorporation kinetics of pyruvate (C), lactate (D), serine
592 (E), glycine (F), alanine (G) and citrate (H) in *Olfr2* KO, *Gpi1* KO, or koningic acid (KA)-
593 treated npTh17 cells by GC-MS.
594 (I) Intracellular abundance of pyruvate, lactate, alanine, serine, glycine and citrate in targeted
595 npTh17 cells, as determined by GC-MS. Raw ion counts were normalized to extraction
596 efficiency and cell number. The abundance is shown relative to the *Olfr2* sample set as 100.
597 (J) Quantification of the production flux of serine, glycine, alanine, pyruvate and lactate based on
598 the ^{13}C incorporation kinetics and intracellular abundance of each metabolite. Three
599 replicates for each sample.
600 (K) OCR (top) and Extracellular Acidification Rate (ECAR) (bottom) of targeted or KA-treated
601 npTh17 cells at baseline and in response to oligomycin (Oligo), carbonyl cyanide 4-
602 (trifluoromethoxy) phenylhydrazone (FCCP), and rotenone plus antimycin (R + A). 10
603 replicates for each condition.
604 (L) ATP-linked respiration rate, quantified based on panel K. Data are representative of two
605 independent experiments.
606 P values were determined using t tests.
607
608 **Figure 6. Hypoxia in the inflamed spinal cord of the EAE model restrains mitochondrial**
609 **respiration, leading to the elimination of Gpi1-deficient Th17 cells**
610 (A) Relative number of gRNA-targeted Th17 cells cultured for 120 h *in vitro* in either normoxic
611 (20% O_2) or hypoxic (3% O_2) conditions. Cell number was normalized to *Olfr2* KO (*Olfr2*
612 cell number was set as 100).

613 (B) Representative FACS histogram showing pimonidazole labeling of total $CD4^+$ T cells
614 isolated from the SC and the dLN at day 15 after induction of EAE and from the SILP and
615 the mLN of SFB-colonized mice.
616 (C) Experimental design of the Hif1a bone marrow reconstitution experiment. *Rag1* KO mice
617 were lethally irradiated and reconstituted with equal numbers of bone marrow cells from
618 *Hif1a*$^{+/+}$ *Cd4*^{cre} CD45.1/2 and *Hif1a*$^{f/f}$ *Cd4*^{cre} CD45.1/1 donors. $CD4^+$ T cells were examined
619 2-months later in peripheral blood (PB), after which mice were either gavaged with SFB or
620 immunized for EAE induction, and $CD4^+$ T cells from SC or SILP from each model were
621 isolated at day15 for examination.
622 (D) Top, representative FACS plots showing the frequencies of *Hif1a*$^{+/+}$ *Cd4*^{cre} and *Hif1a*$^{f/f}$*Cd4*^{cre}
623 $CD4^+$ T cells in the peripheral blood and the SILP or the SC of the SFB and the EAE models,
624 respectively. Bottom, compilation of the KO/WT total $CD4^+$ cell number ratio obtained in
625 the PB and the SILP or the SC of the SFB and EAE models. Two experiments were
626 performed with the same conclusion.
627 (E) Time-course of 2D2 cas9 co-transfer experiment. Left, representative FACS plot showing the
628 frequencies of the *Olfr2* control and the co-transferred *Olfr2* or *Gpi1* KO 2D2 cells in total
629 $CD4^+$ T cells isolated from the dLN or the SC at different time points of EAE. Right,
630 compilation of the KO/Olfr2 control cell number ratio in the dLN or the SC. Data are
631 representative of two independent experiments.
632 (F) EDU in vivo labeling of co-transferred 2D2 cells in the EAE model. Left, representative
633 FACS plots showing the frequencies of EDU^+ among co-transferred *Olfr2* control and *Gpi1*
634 KO 2D2 cells in the SC at the onset of EAE (day10). Middle, compilation of the percentage

635 EDU$^+$ cells in the *Olfr2* control and the *Gpi1* KO cells. Right, the *Gpi1* KO/*Olfr2* control
636 ratios of percentage EDU$^+$ cells. Two experiments were performed with the same conclusion.
637 P values were determined using t tests. Panel D, F, and Day13 dLN and SC comparison in panel
638 E were analyzed with paired t tests.
639 See also Figure S6.
640
641 **Supplemental figure titles and legends**
642 **Figure S1. Single cell RNAseq analysis of ex vivo CD4$^+$ T cells from spinal cord in the EAE**
643 **model and the SILP of SFB-colonized mice, related to Figure 1**
644 (A) Experimental design of the scRNAseq analysis. Lethally irradiated *Rag1* KO mice were
645 reconstituted with equal numbers of bone marrow cells from isotype-marked *Il23r*$^{Gfp/+}$ and
646 *Il23r*$^{Gfp/Gfp}$ donors. The CD4$^+$ T cells of both *Il23r* het and KO background in the SC and
647 SILP of each model were sorted for scRNAseq analysis.
648 (B, C) UMAP projections of the scRNAseq data showing the five CD4$^+$ T cell sub-populations in
649 the SILP of SFB colonized mice and the four sub-populations in the SC of EAE mice.
650 (D, E) Violin plots showing the expression level of selected marker genes for each cluster in the
651 SFB model (D) and the EAE model (E).
652 (F, G) Distribution of *Il23r*$^{Gfp/+}$ and *Il23r*$^{Gfp/Gfp}$ cells in the UMAP projection of SILP CD4$^+$ T
653 cells (F) and EAE SC CD4$^+$ T cells (G).
654 (H) Pie chart showing the percentage of *Il23r*^{het} and *Il23r*^{KO} cells in each cluster as in panels D-
655 G. The total number of *Il23r*$^{Gfp/+}$ cells is scaled according to that of *Il23r*$^{Gfp/Gfp}$ cells for the
656 analysis (assuming same number of heterozygous and homozygous cells were analyzed).
657 The actual cell number of each cluster is indicated beneath the corresponding chart.

658 (I) Validation of marker gene expression in EAE clusters shown in panel E. Top, Klrc1 and
659 Klrd1 are co-expressed on cells that mainly produce IFN-γ (left), but are not expressed on
660 Treg cells (right), and are thus considered as Th1* (IFN-γ producing pathogenic Th17)
661 markers. Bottom left, Treg cells express less Rankl (encoded by *Tnfsf11*). Bottom right,
662 majority of the IFN-γ- and IL-17a-producing cells are Rankl^{+}.
663 (J, K) Pathway enrichment analysis showing the top 2 pathways activated in EAE-associated
664 Th17 (J) or Th1* (K) cells compared to SFB-induced Th17 cells.
665 (L, M) Volcano plots based on the scRNAseq analysis showing the differentially expressed
666 genes in EAE-associated Th17 (L) or Th1* cells (M) compared to SFB-induced Th17 cells.
667 Genes selected for functional screening are highlighted.
668
669 **Figure S2. Tpi1 is essential for EAE-associated Th17 cell pathogenicity, related to Figure 1**
670 **and STAR Methods**
671 (A) Schematic of the PSIN retroviral vector encoding the Thy1.1 reporter and two gRNAs.
672 (B) Knockout efficiency with single compared to double gRNA vectors. In vitro cultured CD4^{+} T
673 cells were infected with the retrovirus containing a single or two gRNAs targeting *Cd4,* and
674 Cd4 expression was evaluated 72 h later.
675 (C) Experimental design for functional screening of pathogenic genes in the transfer EAE model.
676 Naïve 2D2 Cas9 CD4^{+} T cells were activated in vitro, infected with the double gRNA
677 retrovirus, and differentiated into Th17 cells. Thy1.1 high cells were purified and transferred
678 into *Rag1* KO mice (50k cells/mouse), which were immunized with MOG/CFA at the same
679 time. EAE progression was monitored to evaluate the requirement for each gene in
680 pathogenesis.

681 (D) Clinical disease course of EAE in *Rag1* KO mice receiving control *(Olfr2* KO) 2D2 cells or
682 candidate gene KO 2D2 cells, and in MOG-CFA-immunized *S100a4* KO and WT littermate
683 control mice (6 pairs). The 2D2 transfer system was validated by failure of 2D2 cells
684 deficient in *Bhlhe40*, a gene known to be essential for T cell pathogenicity, to induce EAE.
685 At least 5 mice were used for each group, and each experiment was repeated at least twice.
686 (E, F) Sorting strategy for bulk RNAseq analysis of EAE-associated Th17, Th1*, Treg (E)
687 and SFB-induced Th17 and Treg cells (F).
688
689 **Figure S3. *Tpi1* is essential for the differentiation of all CD4$^+$ T cells, related to Figure 1**
690 (A, B) Impaired RORγt, Foxp3, IL-17a and IFN-γ expression by *Tpi1* mutant compared to WT
691 CD4$^+$ T cells in the mLN (A) and the SILP (B) of reconstituted mixed bone marrow chimeric
692 mice colonized with SFB. Left panels, representative FACS plots showing RORγt/Foxp3 and
693 IL-17a/IFN-γ expression in paired *Tpi1* WT (red) and KO (blue) CD4$^+$ T cells in each mouse.
694 Middle panels, frequencies of each CD4$^+$ T cell subtype among the *Tpi1* WT and *Tpi1* KO
695 cells. Right panels, *Tpi1* KO/*Tpi1* WT ratios for each CD4$^+$ T cell subtype in mLN and SILP.
696 (C) Impaired RORγt, Foxp3, IL-17a and IFN-γ expression in *Tpi1* mutant compared to WT CD4$^+$
697 T cells in the dLN of mixed bone marrow reconstituted mice, at day 15 of MOG-induced
698 EAE. The number of *Tpi1* KO CD4$^+$ T cells obtained from SC was too low for a meaningful
699 subtype analysis, and hence is not shown. Panels are organized as in (B).
700
701 **Figure S4. Electroporation-based CRISPR-mediated targeting of metabolic genes in naïve**
702 **CD4$^+$ T cells, related to Figure 2 and STAR Methods**

703 (A) Map of metabolic pathways, showing relevant genes and metabolites in glycolysis, PPP and
704 the TCA cycle. The biosynthetic processes from glycolysis metabolites are labeled in green.
705 Genes that were targeted using CRISPR in this study are labeled in blue. Gpi1, Tpi1 and
706 Ldha are the three enzymes that are expected to not be essential for glycolysis: (1) The
707 reaction catalyzed by Gpi1 (glucose-6-phosphate to fructose-1,6-bisphosphate) can also be
708 achieved by the PPP, making Gpi1 possibly redundant for this reaction; (2) Tpi1 controls the
709 inter conversion of glyceraldehyde-3-phosphate and dihydroxyacetone phosphate, the two 3-
710 carbon molecules generated by degrading fructose-1,6-phosphate. Loss of Tpi1 should lead
711 to the loss of 50%, but not all of the glycolytic activity, and thus may be not lethal; (3) Ldha
712 controls the conversion of pyruvate to lactic acid, and the regeneration of NAD^+. However,
713 pyruvate could still enter the TCA cycle in Ldha-deficient cells, for energy production and
714 biomass synthesis.
715 (B) Schematic of gene targeting in naïve T cells. Left, PCR amplicons encoding gRNAs were
716 electroporated into Cas9-expressing naïve $CD4^+$ T cells, which were subsequently cultured in
717 vitro or transferred into recipient mice. Right, *in vivo* KO efficiency can be assessed by
718 measuring the KO efficiency of the in vitro cultured Th17 cells. Cas9-expressing 7B8 naïve
719 $CD4^+$ T cells were electroporated with *Gfp* guide amplicons to target the Gfp that is co-
720 expressed with Cas9 at the Rosa26 locus, and then cultured *in vitro* in Th17 conditions
721 (IL6+TGF-β), or transferred into SFB-colonized mice. Gfp expression was examined 4 days
722 later in the in vitro cultured Th17 cells (top) and the ex vivo cells isolated from the mLN
723 (bottom).
724 (C-E) Evaluation of the knockout efficiency of guides used in this study with in vitro Th17 cell
725 culture. 8000 electroporated naïve $CD4^+$ T cells were seeded in each well at the beginning of

726 Th17 cell culture. Because gene function is related to cell growth and differentiation, we
727 estimated the KO efficiency based on three variable factors at 120 h post electroporation:
728 protein expression level (C), live cell number (D), and IL-17a production (E). Taking *Gapdh*
729 targeting as an example, western blot data shows Gapdh protein expression decreased only
730 ~40%. However, the cell number was reduced ~70%, and IL-17a production by live cells was
731 further reduced more than 50% compared to the *Olfr2* control. Taken together, we estimate
732 that the Gapdh guide achieved more than 80% knockout *in vitro*. Data are representative of
733 three independent experiments.
734 (F) Efficiency of gene inactivation following electroporation of naïve Cas9 $CD4^+$ T cells with a
735 mixture of two guide amplicons targeting *Cd4* and *Cd45* in cultured Th17 cells at 96 h.
736 P values were determined using t tests.
737
738 **Figure S5. Differentiation of glycolysis gene-targeted 7B8 T cells in the SILP of SFB-**
739 **colonized mice, related to Figure 2**
740 (A) Representative FACS plots showing the expression of RORγt and Foxp3 in the *Olfr2* KO
741 control cells and the co-transferred *Olfr2* control or glycolysis gene KO cells in the SILP at
742 day 15 post transfer.
743 (B) Left, summary of the Th17 frequencies ($ROR\gamma t^+$ $Foxp3^-$) in the *Olfr2* KO control cells
744 (green) and the co-transferred *Olfr2* control or glycolysis gene KO cells (red), as in panel
745 (A). Right, the KO/Olfr2 ratios of Th17 frequencies.
746 (C) Representative FACS plots showing IL-17a expression in *Olfr2* control and co-transferred
747 *Olfr2* control or glycolysis gene KO Th17 cells ($ROR\gamma t^+$ $Foxp3^-$ cells) isolated from the SILP
748 at day 15 post transfer and following *in vitro* PMA/Ionomycin re-stimulation.

749 (D) Left, summary of IL-17a expression based on results in panel (C). Right, KO/*Olfr2* ratios of
750 IL-17a expression. There was consistent reduction of IL-17a in *Gpi1- or Ldha*-targeted, but
751 not in *Olfr2*-targeted 7B8 cells isolated from the SILP and re-stimulated in vitro. While the
752 reduced cytokine production observed in the *in vitro* restimulation assay supports the
753 maintainence of Gpi1-deficient cells in the SILP, it is not necessarily contradictory to our
754 previous claim that Gpi1-deficient 7B8 cells produce normal amounts of IL-17a (based on
755 Il17a$^{GFP/+}$ assay (Figure 2H)), as *in vitro* restimulation was conducted in an artificial
756 microenvironment with strong stimuli, wheareas *Il17a*$^{GFP/+}$ reporter cells report the true
757 cytokine production in real physiological conditions.
758 P values were determined using t tests.
759
760 **Figure S6. Hypoxic microenvironment in the EAE spinal cord impairs proliferation of**
761 ***Gpi1*-deficient Th17 cells, related to Figure 6**
762 (A, B) The PPP contributes to Th17 cell accumulation in the SC in EAE. (A) Representative
763 FACS plots showing the frequencies of co-transferred *Olfr2* KO and *Olfr2* control or *G6pdx*
764 KO 2D2 T cells in the EAE SC at day 15. (B) Compilation of KO/*Olfr2* cell number ratios as
765 shown in panel A.
766 (C) Lactate secretion of *in vitro* cultured *Olfr2* and *Gpi1* KO npTh17 cells in normoxia and
767 hypoxia. Cells were cultured as in Figure 3A in normoxia. At 96 h cells were re-plated in
768 new wells with fresh npTh17 medium in normoxia and hypoxia, and supernatants were
769 collected 12 h later for lactate quantification by GC-MS.
770 (D) Relative intracellular ATP abundance of in vitro cultured Olfr2 and Gpi1 KO npTh17 cells
771 in normoxia and hypoxia. Cells were cultured as in Figure 3A in normoxic condition. At 96 h

772 cells were re-plated in new wells with fresh npTh17 medium in normoxic and hypoxic
773 condition, and ATP level was measured 12 h later.
774 (E, F) Pimonidazole staining of different $CD4^+$ T cell subsets in the SFB and EAE models. (E)
775 Representative FACS plots showing pimonidazole staining of each subtype of $CD4^+$ T cell in
776 the mLN and the SILP of SFB-colonized healthy mice and in the dLN and the SC of EAE
777 mice. Treg ($Foxp3^+$ $ROR\gamma t^-$ $Tbet^-$), Th17 ($ROR\gamma t^+$ $Foxp3^-Tbet^-$), Th1 ($Tbet^+$ $ROR\gamma t^-$ $Foxp3^-$),
778 $Triple^-$ ($ROR\gamma t^-$ $Tbet^-$ $Foxp3^-$). (F) Summarized pimonidazole staining based on panel C.
779 (G) Transcription factor staining in $CD4^+$ T cells from *Hif1a* WT and KO mice colonized with
780 SFB (top, cells from SILP)) or subjected to EAE (bottom, from SC at day15). Left,
781 representative FACS plots showing the frequencies of Th17 cells ($ROR\gamma t^+$ $Foxp3^-$) and Treg
782 cells ($Foxp3^+$ $ROR\gamma t^-$) among total *Hif1a* WT and KO $CD4^+$ T cells; Right, summary of
783 transcription factor staining from two independent experiments.
784 (H) Cytokine production in $CD4^+$ T cells from *Hif1a* WT and KO CD4 T cells in the SFB (top)
785 and EAE (bottom) models after in vitro PMA/ionomycin restimulation. Left, representative
786 plots showing the frequencies of IL-17a producing cells among $ROR\gamma t^+$ $Foxp3^-$ *Hif1a* WT or
787 KO cells in the SILP of SFB-colonized mice (top) and frequencies of IL-17a, IL-17a/IFN-γ,
788 and IFN-γ producing cells among $Foxp3^-$ *Hif1a* WT or KO cells in the SC at day 15 after
789 EAE induction (bottom); Right, summary of cytokine production from two independent
790 experiments. .
791 (I) Left, representative plots showing EDU incorporation in co-transferred *Olfr2* and *Olfr2*
792 control or *Gpi1* KO 2D2 cells at different days post transfer in the dLNs. Right, compiled
793 data of one representative experiment. Two independent experiments were performed with
794 the same conclusion.

795 (J, K) Proliferation of dLN 2D2 cells in the EAE model and mLN 7B8 cells in SFB-colonized
796 mice. Naïve 7B8 or 2D2 $CD4^+$ T cells were labeled with CFSE and 100K cells were
797 transferred into recipient mice that had been previously colonized with SFB or were
798 immunized with MOG/CFA immediately after cell transfer. The mLN of the 7B8 model and
799 dLN of the EAE model were collected at different time points for cell division analysis. (J)
800 Left, representative FACS plot showing CFSE labeling of the 7B8 and 2D2 cells at different
801 time points. Right, pie charts showing the frequencies of cells with different numbers of
802 divisions. Division number was labeled in different colors. (K) Total cell number count of
803 mLN 7B8 cells and dLN 2D2 cells at different time points. For each time point, 4-10 mice
804 were used for each group. Two independent experiments were performed with the same
805 conclusion.
806 (L, M) IL-17a production (L) and RORγt/Foxp3 expression (M) in 2D2 cells from dLN at day 10
807 in the EAE model. Left, representative FACS plots showing the overlay of IL-17a expression
808 (L) or RORγt/Foxp3 expression (M) in *Olfr2* control and co-transferred *Olfr2* KO or *Gpi1*
809 KO 2D2 cells. Middle, compilation of frequencies of IL-$17a^+$ (L) or $ROR\gamma t^+Foxp3^-$ cells (M)
810 among *Olfr2* control and co-transferred *Olfr2* KO or *Gpi1* KO 2D2 cells. Right, the
811 KO/Olfr2 ratios of the IL-$17a^+$ frequencies (L) and $ROR\gamma t^+Foxp3^-$ frequencies (M).
812 (N, O) Left, compiled data showing the frequencies of $Ccr6^+$ cells among co-transferred *Olfr2*
813 and *Olfr2* control or *Gpi1* KO 2D2 cells in the dLN at day 9 (N) or in the SC at day 13 (O)
814 post transfer and EAE induction. Right, the KO/Olfr2 ratios of the $Ccr6^+$ frequencies. Two
815 independent experiments were performed with the same conclusion.

816 (P) Compiled data showing the frequencies of active Caspase3^{+} cells among co-transferred *Olfr2*

817 and *Olfr2* control or *Gpi1* KO 2D2 cells in the SC at day 10 post transfer and EAE induction.

818 n=10.

819 P values of panel B, C, D, K, L, M, N, and O were determined using t tests. P values of panel G,

820 H, and P, were determined using paired t tests.

821

822 # STAR Methods

823 # RESOURCE AVAILABILITY

824

825 ## LEAD CONTACT AND MATERIALS AVAILABILITY

826 Further information and requests for resources and reagents should be directed to and will be

827 fulfilled by the Lead Contact, Dan R. Littman (Dan.Littman@med.nyu.edu).

828

829 ### Materials Availability

830 This study did not generate new unique reagents

831

832 ### Data and Code Availability

833 The bulk RNAseq data and the scRNA seq data supporting the current study have been deposited

834 in GEO (accession number GSE141006).

835

836 # EXPERIMENTAL MODEL AND SUBJECT DETAILS

837 ### Mouse Strains

838 C57BL/6 mice were obtained from Taconic Farms or the Jackson Laboratory. All transgenic
839 animals were bred and maintained in the animal facility of the Skirball Institute (NYU School of
840 Medicine) in specific-pathogen-free (SPF) conditions. *Il-23r*^{GFP} mice (Awasthi et al., 2009) were
841 provided by M. Oukka. *S100a4* knockout mice (Li et al., 2010) were provided by Dr. Anne R.
842 Bresnick. *Cas9*^{Tg} mice (Platt et al., 2014) were obtained from Jackson Laboratory (JAX;
843 B6J.129(Cg)-Gt(ROSA)26Sortm1.1(CAG-cas9*,-EGFP)Fezh/J), and maintained on the Cd45.1
844 background (JAX; B6. SJL-Ptprca Pepcb/BoyJ). SFB-specific TCRTg (7B8) mice (Yang et al.,
845 2014), MOG-specific TCRTg (2D2) mice (Bettelli et al., 2003), and *Helicobacter hepaticus*-
846 specific TCRTg (HH7-2) mice (Xu et al., 2018) were previously described. They were crossed to
847 the Cas9^{Tg} Cd45.1/1 mice to generate 7B8 *Cas9* ^{Tg}, 2D2 *Cas9* ^{Tg}, and HH7-2 *Cas9* ^{Tg} mice with
848 either Cd45.1/1 or Cd45.1/2 congenic markers. 7B8 Cas9 CD45.1/2 mice were further crossed
849 with *IL17a*$^{GFP/GFP}$ reporter mice (JAX; C57BL/6-Il17atm1Bcgen/J) to generate 7B8 *Cas9*
850 *IL17a*$^{GFP/+}$ Cd45.1/2 or Cd45.2/2 mice. Female *Foxp3*$^{RFP/RFP}$ reporter mice (Jax; C57BL/6-
851 Foxp3^{tm1Flv}/J) were crossed with male *IL17a*$^{GFP/GFP}$ reporter mice to generate *IL17a*$^{GFP/+}$
852 *Foxp3*^{RFP} male mice for bulk RNAseq. *Hif1a*$^{f/f}$ mice (Jax; B6.129-Hif1a^{tm3Rsjo}/J) were crossed
853 with *CD4*^{cre} mice (Jax; B6.Cg-Tg(Cd4-cre)1Cwi/BfluJ) and CD45.1/1 mice to generate *Hif1a*$^{+/+}$
854 *CD4*^{cre} CD45.1/1 and *Hif1a*$^{f/f}$ *CD4*^{cre} CD45.2/2 littermates. *Tpi1*$^{f/+}$ mice generated by crossing
855 *Tpi1*$^{tm1a(EUCOMM)Wtsi}$ mice (Wellcome Trust Sanger Institute; B6Brd;B6N-Tyr^{c-Brd}
856 Tpi1$^{tm1a(EUCOMM)Wtsi}$/WtsiCnbc) with a FLP deleter strain (Jax; B6.129S4-
857 Gt(ROSA)26Sor$^{tm1(FLP1)Dym}$/RainJ) were further crossed with CD4^{cre} and CD45.1/1 strains to
858 generate *Tpi1*$^{+/+}$*Cd4*^{cre} and *Tpi1*$^{f/f}$*CD4*^{cre} mice with different congenic markers.
859

860 **METHOD DETAILS**

861 **Flow cytometry**

862 For transcription factor and cytokine staining of *ex vivo* cells, single cell suspensions were
863 incubated for 3h in RPMI with 10% FBS, phorbol 12-myristate 13-acetate (PMA) (50 ng/ml;
864 Sigma), ionomycin (500 ng/ml;Sigma) and GolgiStop (BD). Cells were then resuspended with
865 surface-staining antibodies in HEPES-buffered HBSS. Staining was performed for 20-30 min on
866 ice. Surface-stained cells were washed and resuspended in live/dead fixable blue (ThermoFisher)
867 for 5 min prior to fixation. Cells were treated using the FoxP3 staining buffer set from
868 eBioscience according to the manufacturer's protocol. Intracellular stains were prepared in 1X
869 eBioscience permwash buffer containing anti-CD16/anti-CD32, normal mouse IgG, and normal
870 rat IgG Staining was performed for 30-60 min on ice.

871

872 For cytokine analysis of *in vitro* cultured Th17 cells, cells were incubated in the restimulation
873 buffer for 3 h. After surface and live/dead staining, cells were treated using the
874 Cytofix/Cytoperm buffer set from BD Biosciences according to the manufacturer's protocol.
875 Intracellular stains were prepared in BD permwash in the same manner used for transcription
876 factor staining. Flow cytometric analysis was performed on an LSR II (BD Biosciences) or an
877 Aria II (BD Biosciences) and analyzed using FlowJo software (Tree Star).

878

879 **Retroviral transduction and 2D2 TCRtg Cas9^{Tg} T cell-mediated EAE**

880 The protocol described in this section was only used for experiments shown in Figure 2F and
881 Figure S2A-D. sgRNAs were designed using the Crispr guide design software
882 (http://crispr.mit.edu/). sgRNA encoding sequences were cloned into the retroviral sgRNA
883 expression vector pSIN-U6-sgRNAEF1as-Thy1.1-P2A-Neo that has been reported before (Ng et

884 al., 2019). To make the double sgRNA vector for experiments shown in Figures S2A-D, the
885 sgRNA transcription cassette, ranging from the U6 promoter to the U6 terminator, was amplified
886 (primer sequences can be found in the Key Resources Table) and cloned into the pSIN vector
887 after the first sgRNA encoding cassette. For the EAE experiment shown in Figure 2F, only one
888 sgRNA was used for each virus. Retroviruses were packaged in PlatE cells by transient
889 transfection using TransIT 293 (Mirus Bio).
890
891 Tissue culture plates were coated with polyclonal goat anti-hamster IgG (MP Biomedicals) at
892 37 °C for at least 3 h and washed 3× with PBS before cell plating. FACS-sorted
893 $CD4^{+}CD8^{-}CD25^{-}CD62L^{+}CD44^{low}$ naïve 2D2 TCRtg *Cas9*^{Tg} T cells were seeded for 24 h in T
894 cell medium (RPMI supplemented with 10% FCS, 2mM β-mercaptoethanol, 2mM glutamine),
895 along with anti-CD3 (BioXcell, clone 145-2C11, 0.25µg/ml) and anti-CD28 (BioXcell, clone
896 37.5.1, 1µg/ml) antibodies. Cells were then transduced with the pSIN virus by spin infection
897 at 1200 × g at 30 °C for 90 min in the presence of 10µg/ml polybrene (Sigma). Viral
898 supernatants were removed 12 h later and replaced with fresh medium containing anti-
899 CD3/anti-CD28, 20ng/ml IL-6 and 0.3ng/ml TGF-β. Cells were lifted off 48 h later and
900 supplemented with IL-2 for another 48hours. Thy1.1^{high} cells were then sorted with the ARIA
901 and i.v. injected into *Rag1*$^{-/-}$ mice (50k cells/mouse). Mice were then immunized
902 subcutaneously on day 0 with 100µg of MOG_{35-55} peptide, emulsified in CFA (Complete
903 Freund's Adjuvant supplemented with 2mg/mL *Mycobacterium tuberculosis* H37Ra), and
904 injected i.p. with 200 ng pertussis toxin (Calbiochem). The EAE scoring system was as follows:
905 0-no disease, 1-Partially limp tail; 2-Paralyzed tail; 3-Hind limb paresis, uncoordinated
906 movement; 4-One hind limb paralyzed; 5-Both hind limbs paralyzed; 6-Hind limbs paralyzed,

907 weakness in forelimbs; 7-Hind limbs paralyzed, one forelimb paralyzed; 8-Hind limbs paralyzed,
908 both forelimbs paralyzed; 9-Moribund; 10-Death.
909
910 **sgRNA guide amplicon electroporation of naïve CD4$^+$ T cells**

911 sgRNA-encoding sequences were cloned into the pSIN vector (single sgRNA in one vector).
912 The sgRNA encoding cassette, ranging from the U6 promoter to the U6 terminator, was
913 amplified with 34 cycles of PCR with Phusion (NEB), and purified with Wizard SV Gel and
914 PCR Clean-up System (Promega), and concentrated with a standard ethanol DNA
915 precipitation protocol. Amplicons were resuspended in a small volume of H_2O and kept at -
916 80 °C until use. Amplicon concentration was measured with Qubit dsDNA HS assay kit
917 (Thermofisher)
918
919 The Amaxa P3 Primary Cell 4D-Nucleofector X kit was used for T cell electroporation. 2
920 million FACS-sorted naïve CD4$^+$ *Cas9*^{Tg} cells were pelleted and resuspended in 100ul P3
921 primary cell solution supplemented with 0.56ug sgRNA amplicon (for single gene knockout),
922 or equal amounts of sgRNA amplicons (0.56ug each for targeting two genes simultaneously in
923 Figures 3D, and 4E). For GFP KO (Figure S4B), a mixture of three pSIN vectors at equal
924 amount containing different sgRNA-encoding sequences (all targeting GFP) was used as
925 template for PCR amplifaction, and 0.56ug of amplicon was used for electroporation. Cell
926 suspensions were transferred into a Nucleocuvette Vessel for electroporation in the
927 Nucleofector X unit, using program "T cell. Mouse. Unstim.". Cells were then rested in 500 ul
928 mouse T cell nucleofector medium (Lonza) for 30 min before in vitro culture or transfer into
929 mice.

930

931 In vitro cell culture – 96 well flat-bottom tissue culture plates (Corning) were coated with
932 polyclonal goat anti-hamster IgG (MP Biomedicals) at 37 °C for at least 3 h and washed 3×
933 with PBS before cell plating. Electroporated cells were plated into each well containing 200ul
934 T cell culture medium (glucose-free RPMI (ThermoFisher) supplemented with 10% FCS
935 (Atlanta Biologicals), 4g/L glucose, 4mM glutamine, 50uM β-mercaptoethanol, 0.25μg/ml
936 anti-CD3 (BioXcell, clone 145-2C11) and 1μg/ml anti-CD28 (BioXcell, clone 37.5.1)
937 antibodies). For npTh17 culture, 20ng/ml IL-6 and 0.3ng/ml TGF- β were further added into
938 the T cell medium. For pTh17 cell culture, 20ng/ml IL-6, 20ng/ml IL-23, and 20ng/ml IL-1β
939 were further added into the T cell medium. Cells were then cultured for 96 h or 120 h in
940 normoxia or hypoxia (3% oxygen) before metabolic experiments or cell number
941 counting/western/FACS profiling, respectively.

942

943 T cell transfer into mice – TCR transgenic *Cas9*^{Tg} naïve CD4^{+} T cells (7B8 TCRtg for SFB
944 model, 2D2 TCRtg for EAE model, and HH7-2 TCRtg for colitis model) with different
945 isotype markers were electroporated at the same time. Equal numbers of isotype-distinct
946 electroporated resting cells were mixed, pelleted and resuspended in dPBS supplemented with
947 1% filtered FBS before retro-orbital injection into recipient mice (100,000 cells in total for
948 each mouse). The transferred cells were isolated from SILP of the SFB model, SC of the EAE
949 model, and the LILP of the colitis model at day 15 post transfer, unless otherwise indicated.

950

951 **SFB model**

952 C57BL/6 mice were purchased from Jackson Laboratory and maintained in SFB-free SPF cages.
953 Fresh feces of SFB mono-colonized mice maintained in our gnotobiotic animal facility were
954 collected and frozen at -80 °C until use. Fecal pellets were meshed through a 100uM strainer
955 (Corning) in cold sterile dPBS (Hyclone). 300 µl feces suspension, equal to the amount of 1/3
956 pellet, was administered to each mouse by oral gavage. Mice were inoculated one more time at 24
957 h. For the transfer experiment, electroporated cells were injected 96 h after the initial gavage.
958

959 **Colitis model**

960 *H. hepaticus* was provided by J. Fox (MIT) and grown on blood agar plates (TSA with 5% sheep
961 blood, Thermo Fisher) as previously described (Xu et al., 2018). Briefly, *Rag1*$^{-/-}$ mice were
962 colonized with *H. hepaticus* by oral gavage on days 0 and 4 of the experiment. At day 7,
963 electroporated naïve HH7-2 TCRtg *Cas9*^{Tg} CD4^{+} T cells were adoptively transferred into the *H.*
964 *hepaticus*-colonized recipients. In order to confirm *H. hepaticus* colonization, *H. hepaticus*-
965 specific 16S primers were used on DNA extracted from fecal pellets. Universal 16S were
966 quantified simultaneously to normalize *H. hepaticus* colonization of each sample.
967

968 **EAE model**

969 Right after the transfer of electroporated 2D2 *Cas9*^{Tg} cells, mice were immunized subcutaneously
970 on day 0 with 100µg of MOG_{35-55} peptide, emulsified in CFA (Complete Freund's Adjuvant
971 supplemented with 2mg/mL Mycobacterium tuberculosis H37Ra), and injected i.p. on days 0
972 and 2 with 200 ng pertussis toxin (Calbiochem).
973

974 **Isolation of lymphocytes from lamina propria, spinal cord, and lymph nodes**

975 For isolating mononuclear cells from the lamina propria, the intestine (small and/or large) was
976 removed immediately after euthanasia, carefully stripped of mesenteric fat and Peyer's
977 patches/cecal patch, sliced longitudinally and vigorously washed in cold HEPES buffered
978 (25mM), divalent cation-free HBSS to remove all fecal traces. The tissue was cut into 1-inch
979 fragments and placed in a 50ml conical containing 10ml of HEPES buffered (25mM), divalent
980 cation-free HBSS and 1 mM of fresh DTT. The conical was placed in a bacterial shaker set to
981 37 °C and 200rpm for 10 minutes. After 45 seconds of vigorously shaking the conical by hand,
982 the tissue was moved to a fresh conical containing 10ml of HEPES buffered (25mM), divalent
983 cation-free HBSS and 5 mM of EDTA. The conical was placed in a bacterial shaker set to 37 °C
984 and 200rpm for 10 minutes. After 45 seconds of vigorously shaking the conical by hand, the
985 EDTA wash was repeated once more in order to completely remove epithelial cells. The tissue
986 was minced and digested in 5-7ml of 10% FBS-supplemented RPMI containing collagenase (1
987 mg/ml collagenaseD; Roche), DNase I (100 µg/ml; Sigma), dispase (0.05 U/ml; Worthington)
988 and subjected to constant shaking at 155rpm, 37 °C for 35 min (small intestine) or 55 min (large
989 intestine). Digested tissue was vigorously shaken by hand for 2 min before adding 2 volumes of
990 media and subsequently passed through a 70 µm cell strainer. The tissue was spun down and
991 resuspended in 40% buffered percoll solution, which was then aliquoted into a 15ml conical. An
992 equal volume of 80% buffered percoll solution was underlaid to create a sharp interface. The
993 tube was spun at 2200rpm for 22 min at 22 °C to enrich for live mononuclear cells. Lamina
994 propria (LP) lymphocytes were collected from the interface and washed once prior to staining.

995 For isolating mononuclear cells from spinal cords during EAE, spinal cords were mechanically
996 disrupted and dissociated in RPMI containing collagenase (1 mg/ml collagenaseD; Roche),

997 DNase I (100 µg/ml; Sigma) and 10% FBS at 37 °C for 30 min. Leukocytes were collected at the
998 interface of a 40%/80% Percoll gradient (GE Healthcare).

999 For isolating mononuclear cells from lymph nodes, mesenteric lymph nodes (for the SFB
1000 model), and draining lymph nodes (Inguinal, axillary, and brachial lymph nodes for the EAE
1001 model) were mechanically dissected and minced in RPMI containing 10% FBS and 25mM
1002 HEPES through 40uM strainer. Cells were collected for further analysis.
1003

1004 **Generation of bone marrow chimeric reconstituted mice**

1005 Bone marrow mononuclear cells were isolated from donor mice by flushing the long bones. To
1006 generate *Tpi1*^{WT}/ *Tpi1*^{KO} chimeric reconstituted mice, *Tpi1*$^{+/+}$ *Cd4*^{Cre} CD45.1/2 and *Tpi1*$^{f/f}$ *Cd4*^{Cre}
1007 CD45.2/2 mice were used as donors. To generate *Hif1a*^{WT}/*Hif1a*^{KO} chimeric reconstituted mice,
1008 *Hif1a*$^{+/+}$ *Cd4*^{Cre} CD45.1/2 and *Hif1a*$^{f/f}$ *Cd4*^{Cre} CD45.1/1 mice were used as donors. To generate
1009 *Il23r*^{het}/*Il23r*^{KO} chimeric reconstituted mice, *Il23r*$^{Gfp/+}$ CD45.1/2 *and Il23r*$^{Gfp/Gfp}$ CD45.1/1 mice
1010 were used as donors. Red blood cells were lysed with ACK Lysing Buffer, and CD4/CD8 T
1011 cells were labeled with CD4/CD8 magnetic microbeads and depleted with a Miltenyi LD
1012 column. The remaining cells were resuspended in PBS for injection in at a 1:1 ratio (WT: KO).
1013 4×10^6 cells were injected intravenously into 6 week old mice (CD45.1/1 in Tpi1 experiment;
1014 Rag1$^{-/-}$ in Hif1a experiment) that were irradiated 4h before reconstitution using 1000 rads/mouse
1015 (2x500rads, at an interval of 3h, at X-RAD 320 X-Ray Irradiator). Peripheral blood samples
1016 were collected and analyzed by FACS 8 weeks later to check for reconstitution, after which SFB
1017 colonization or EAE induction were performed.
1018

1019 **Pimonidazole HCl labeling**

1020 Pimonidazole HCl (hypoxyprobe) was retro orbitally injected into mice at the dose of 100mg/kg
1021 under general anesthesia (Ketamine 100mg/Kg, Xylazine 15mg/Kg). 3 h later, tissues were
1022 dissected and processed to get the mononuclear cell fraction. After surface/live/dead staining,
1023 cells were treated using the FoxP3 staining buffer set from eBioscience according to the
1024 manufacturer's protocol. Intracellular staining with anti-RORγt, Foxp3, Tbet, and biotin-
1025 pimonidazole adduct antibodies were performed for 60min on ice in 1X eBioscience permwash
1026 buffer containing normal mouse IgG (50μg/ml), and normal rat IgG (50μg/ml). The
1027 pimonidazole labeling was visualized with streptavidin APC staining in the same buffer.
1028
1029 **EdU incorporation**
1030 Two doses of EdU (50mg/kg for each) were i.p. injected into MOG/CFA-immunized mice in 12
1031 h intervals at days 4, 6, 8, 9, and 12 post immunization. Draining lymph nodes and/or spinal
1032 cords were dissected 12 h post the second injection. Detection of EdU incorporation into the
1033 DNA was performed with EdU-click 647 Kit (Baseclick) according to the manufacturer's
1034 instructions. In brief, surface-stained cells were fixed in 100μl fixative solution, and
1035 permeabilized in 100μl permeabilization buffer. Cells were pelleted and incubated for 30min in
1036 220μl EdU reaction mixture containing 20μl permeabilization buffer, 20μl buffer additive, 1μl
1037 dye azide, 4μl catalyst solution, and 175μl dPBS, before 3x wash and FACS analysis.
1038
1039 **CFSE labeling**
1040 Sorted naïve 7B8 or 2D2 CD45.1/1 CD4 T cells were stained with CFSE cell proliferation kit
1041 (Life Technology). Labeled cells were administered into each congenic CD45.2/2 recipient
1042 mouse by retro-orbital injection. Mice receiving 7B8 cells were gavaged with SFB mono-feces

1043 twice on days -4 and -3. Mice receiving 2D2 cells were immunized for EAE induction
1044 immediately after cell transfer. mLNs of the SFB-colonized mice were collected at 72h and
1045 120h, and dLN of 2D2-injected mice were collected at 72h, 96h and 120h post transfer for cell
1046 division analysis.
1047
1048 **Bulk RNA sequencing**
1049 Total RNA from sorted target cell populations was isolated using TRIzol LS (Invitrogen)
1050 followed by DNase I (Qiagen) treatment and cleanup with RNeasy Plus Micro kit (Qiagen;
1051 74034). RNA quality was assessed using Pico Bioanalyser chips (Agilent). RNASeq libraries
1052 were prepared using the Clontech Smart-Seq Ultra low RNA kit (Takara Bio) for cDNA
1053 preparation, starting with 550 pg of total RNA, and 13 cycles of PCR for cDNA amplification.
1054 The SMARTer Thruplex DNA-Seq kit (Takara Bio) was used for library prep, with 7 cycles of
1055 PCR amplification, following the manufacturer's protocol. The amplified library was purified
1056 using AMPure beads (Beckman Coulter), quantified by Qubit and QPCR, and visualized in an
1057 Agilent Bioanalyzer. The libraries were pooled equimolarly, and run on a HiSeq 4000, as paired
1058 end reads, 50 nucleotides in length.
1059
1060 **Single cell RNAseq**
1061 Libraries from isolated single cells were generated based on the Smart-seq2 protocol (Picelli et
1062 al., 2014) with the following modifications. In brief, RNA from sorted single cells was used as
1063 template for oligo-dT primed reverse transcription with Superscript II Reverse Transcriptase
1064 (Thermo Fisher), and the cDNA library was generated by 20 cycle PCR amplification with IS
1065 PCR primer using KAPA HiFi HotStart ReadyMix (KAPA Biosystems) followed by Agencourt

1066 AMPure XP bead purification (Beckman Coulter) as described. Libraries were tagmented using
1067 the Nextera XT Library Prep kit (Illumina) with custom barcode adapters (sequences available
1068 upon request). Libraries with unique barcodes were combined and sequenced on a HiSeq2500 in
1069 RapidRun mode, with either 2x50 or 1x50 nt reads.
1070
1071 **Stable-isotope tracing, metabolite secretion and kinetic flux profiling by GC-MS**
1072 *In vitro* cultured np/pTh17 cells were collected at 96h, washed twice in glucose-free RPMI
1073 (ThermoFisher, 11879020) containing 10% dialyzed FBS (ThermoFisher), and re-plated in anti-
1074 hamster IgG-coated 96-well plates at 60,000/well in np/pTh17 medium (glucose-free RPMI
1075 containing 10% dialyzed FBS, 2mM β-mercaptoethanol, 4mM glutamine, anti-CD3, anti-
1076 CD28, and 4g/L isotype labeled glucose). For KA-treated samples, *Olfr2* KO cells were
1077 previously treated with 30 μM KA before collection and re-plating. The re-plated cells were
1078 cultured in Th17 medium supplemented with 30 μM KA.
1079
1080 To measure relative PPP activity, $^{13}C_{1,2}$-glucose (Cambridge Isotope Laboratories) was added
1081 into the Th17 medium. Re-plated cells were further cultured 12 h before metabolite extraction
1082 and GC-MS analysis. After a brief wash with 0.9% ice-cold saline solution to remove media
1083 contamination, cellular metabolites were extracted using a pre-chilled
1084 methanol/water/chloroform extraction method, as previously described (Metallo et al., 2011).
1085 Aqueous and inorganic layers were separated by cold centrifugation for 15 min. The aqueous
1086 layer was transferred to sample vials (Agilent 5190-2243) and evaporated to dryness using a
1087 SpeedVac (Savant Thermo SPD111V).
1088

1089 For lactate secretion analysis, re-plated cells were cultured in normoxia or hypoxia for 12 h.
1090 media was collected and centrifuged at 1,000 x g to pellet cellular debris. 5 µL of supernatant
1091 was extracted in 80% ice-cold methanol mixture containing isotope-labeled internal standards
1092 and evaporated to dryness.
1093
1094 Metabolite abundance [X_m] was determined using the following equation:
1095

1096 $$[X_m] = \frac{X_{std} - \%M0_x}{100 - \%M0_x}$$

1097
1098 where X_{std} is the molar amount of isotope-labeled standard (e.g. 5 nmol lactate) and $\%M0_x$ is the
1099 relative abundance of unlabeled metabolite X corrected for natural isotope abundance.
1100
1101 To quantify the metabolite secretion flux ($Flux_m$), the molar change in extracellular metabolites
1102 was determined by calculating the difference between conditioned and fresh media and
1103 normalizing to changes in cell density:
1104

1105 $$Flux_m = \frac{X_f - X_i}{\int_0^f X_0\, e^{kt}}$$

1106
1107 where X_f and X_i are the final and initial molar amounts of metabolite, respectively, X_0 is the
1108 initial cell density, k is the exponential growth rate (hr^{-1}), and t is the media conditioning time.
1109

1110 For kinetic flux profiling, npTh17 medium was supplemented with 4g/L $^{13}C_6$-glucose
1111 (Cambridge Isotope Laboratories). Cells were collected at various time points. Unlabeled
1112 metabolite (M0) versus time (t) were plotted and the data were fitted to an equation as previously
1113 described (Yuan et al., 2008) to quantify the metabolite turnover rate (t^{-1}):
1114

1115 $$Y = (1 - \alpha)^* \exp(-k^* t) + \alpha$$

1116

1117 where α is the percentage of unlabeled (M0) metabolite at steady-state, k is the metabolite
1118 turnover rate and t is time.
1119

1120 Metabolite flux was quantified by multiplying the decay rate by the intracellular metabolite
1121 abundance.
1122

1123 Metabolite derivatization using MOX-tBDMS was conducted as previously described (Lewis et
1124 al., 2014). Derivatized samples were analyzed by GC-MS using a DB-35MS column (30m x
1125 0.25mm i.d. x 0.25 µm) installed in an Agilent 7890B gas chromatograph (GC) interfaced with
1126 an Agilent 5977B mass spectrometer as previously described (Grassian et al., 2014) and
1127 corrected for natural abundance using in-house algorithms adapted from (Fernandez et al., 1996).
1128

1129 **Intracellular ATP measurement**

1130 npTh17 cells were cultured in vitro in normoxic condition for 96 h before being collected and
1131 washed twice in glucose-free RPMI (ThermoFisher) containing 10% FBS (Atlanta Biologicals),
1132 and re-plated in anti-hamster IgG-coated 96-well plates at 20,000/well in 200µl npTh17 medium

1133 (glucose-free RPMI containing 10% dialyzed FBS, 2mM β-mercaptoethanol, 4mM glutamine,
1134 anti-CD3, anti-CD28, and 4g/L glucose). 12 hours later, cell numbers were determined in
1135 replicate wells, and ATP measurements were made using CellTiter-Glo® Luminescent Cell
1136 Viability Assay kit (Promega) according to instructions.
1137
1138 **LC-MS analysis**
1139 For glucose consumption analysis, supernatants of npTh17 cells, or cell free control, were
1140 collected at 24h post cell re-plating. Metabolites were extracted for LC-MS analysis to measure
1141 glucose and lactate quantities. Glucose consumption rate and lactate production rate was
1142 quantified on a relative basis by calculating the ion count difference between conditioned and
1143 fresh media and normalizing to changes in cell density.
1144
1145 Samples were subjected to an LC-MS analysis to detect and quantify known peaks. A metabolite
1146 extraction was carried out on each sample with a previously described method (Pacold et al.,
1147 2016). In brief, samples were extracted by mixing 10 µL of sample with 490 µL of extraction
1148 buffer (81.63% methanol (Fisher Scientific) and 500 nM metabolomics amino acid mix standard
1149 (Cambridge Isotope Laboratories, Inc.)) in 2.0mL screw cap vials containing ~100 µL of
1150 disruption beads (Research Products International, Mount Prospect, IL). Each was homogenized
1151 for 10 cycles on a bead blaster homogenizer (Benchmark Scientific, Edison, NJ). Cycling
1152 consisted of a 30 sec homogenization time at 6 m/s followed by a 30 sec pause. Samples were
1153 subsequently spun at 21,000 g for 3 min at 4 °C. A set volume of each (360 µL) was transferred
1154 to a 1.5 mL tube and dried down by speedvac (Thermo Fisher, Waltham, MA). Samples were
1155 reconstituted in 40 µL of Optima LC/MS grade water (Fisher Scientific, Waltham, MA).

1156 Samples were sonicated for 2 mins, then spun at 21,000g for 3min at 4°C. Twenty microliters
1157 were transferred to LC vials containing glass inserts for analysis.
1158
1159 The LC column was a MilliporeTM ZIC-pHILIC (2.1 x150 mm, 5 µm) coupled to a Dionex
1160 Ultimate 3000TM system and the column oven temperature was set to 25 °C for the gradient
1161 elution. A flow rate of 100 µL/min was used with the following buffers; A) 10 mM ammonium
1162 carbonate in water, pH 9.0, and B) neat acetonitrile. The gradient profile was as follows; 80-
1163 20%B (0-30 min), 20-80%B (30-31 min), 80-80%B (31-42 min). Injection volume was set to 1
1164 µL for all analyses (42 min total run time per injection).
1165
1166 MS analyses were carried out by coupling the LC system to a Thermo Q Exactive HFTM mass
1167 spectrometer operating in heated electrospray ionization mode (HESI). Method duration was 30
1168 min with a polarity switching data-dependent Top 5 method for both positive and negative
1169 modes. Spray voltage for both positive and negative modes was 3.5kV and capillary temperature
1170 was set to 320°C with a sheath gas rate of 35, aux gas of 10, and max spray current of 100 µA.
1171 The full MS scan for both polarities utilized 120,000 resolution with an AGC target of 3e6 and a
1172 maximum IT of 100 ms, and the scan range was from 67-1000 m/z. Tandem MS spectra for both
1173 positive and negative mode used a resolution of 15,000, AGC target of 1e5, maximum IT of 50
1174 ms, isolation window of 0.4 m/z, isolation offset of 0.1 m/z, fixed first mass of 50 m/z, and 3-
1175 way multiplexed normalized collision energies (nCE) of 10, 35, 80. The minimum AGC target
1176 was 1e4 with an intensity threshold of 2e5. All data were acquired in profile mode.
1177
1178 **Seahorse Analysis**

1179 OCR and ECAR measurements were performed using a Seahorse XFe96 analyzer (Seahorse
1180 Biosciences). Seahorse XFe96 plates were coated with 0.56ug Cell-Tak (Corning) in 24µl
1181 coating buffer (8µl H_2O + 16µl 0.1M $NaHCO_3$ (PH 8.0)) overnight at 4 °C, and washed 3x with
1182 H_2O before use. *In vitro* cultured Th17 cells were collected at 96 h, washed twice in Seahorse
1183 RPMI media PH7.4 (Agilent, 103576-100) and seeded onto the coated plates at 100,000 per well.
1184 To measure the OCR and ECAR of KA-treated cells, 30µM KA (Santa Cruz) was added into
1185 *Olfr2* control Th17 cell samples at the beginning of the Seahorse measurement. Respiratory rates
1186 were measured in RPMI Seahorse media, pH7.4 (Agilent) supplemented with 10 mM glucose
1187 (Agilent) and 2 mM glutamine (Agilent) in response to sequential injections of oligomycin (1
1188 µM) , FCCP (0.5 µM) and antimycin/rotenone (1 µM) (all Cayman Chemicals, Ann Arbor, MI,
1189 USA).
1190

1191 **Western blotting**

1192 Whole cell extracts were fractionated by SDS-PAGE and transferred to nitrocellulose membrane
1193 by wet transfer for 4 h on ice at 60 V. Blots were blocked in TBS blocking buffer (Licor) and
1194 then stained overnight with primary antibody at 4°C. The next day, membranes were washed
1195 three times in TBST (TBS and 0.1% Tween-20), stained with fluorescently conjugated secondary
1196 antibodies (Licor) at 1:10,000 dilution in TBS blocking buffer for 1 h at room temperature, and
1197 then imaged in the 680- and 800-nm channels. Antibodies used: Gapdh (CST), Gpi1 (Thermo
1198 Fisher), Ldha (CST), Pdha1 (Abcam), Tpi1 (Abcam), G6pdx (Abcam), α-tubulin (Santa Cruz).
1199

1200 **QUANTIFICATION AND STATISTICAL ANALYSIS**

1201 **Bulk RNAseq analysis**

1202 Raw reads from bulk RNA-seq were aligned to the mm10 genome using STAR v 2.6.1d with
1203 the quantmode parameter to get read counts. DESeq2 v 1.22.2 was used for differential
1204 expression analysis. Heatmaps were produced using gplots v 3.0.1.1.
1205
1206 **Pre-processing of scRNA-seq data**
1207 The single cell RNA raw sequence reads were aligned to the UCSC Mus musculus genome,
1208 mm10, using Kallisto (Bray et al., 2016). The mean number of reads per cell was 241,500. Gene
1209 expression values were quantified into Transcripts Per Kilobase Million (TPM). We removed
1210 cells which had fewer than 800 detected genes or more than 3,000 genes. After filtering, the
1211 mean number of detected genes per cell were 1,765. Then, for the SFB and EAE dataset, we
1212 normalized the gene matrix by SCTransform (Hafemeister and Satija, 2019) regression with
1213 percent of mitochondria reads separately.
1214
1215 **Visualization and clustering**
1216 To visualize the EAE and SFB data, we performed principal component analysis (PCA) for
1217 dimensionality reduction, and further reduced PCA dimensions into two dimensional space using
1218 UMAP (Becht et al., 2018; McInnes and Healy, 2018). UMAP matrix was also used to build the
1219 weighted shared nearest neighbor graph and clustering of single cells was performed by the
1220 original Louvain algorithm. All the above analysis was performed using Seurat v3 R package
1221 (Butler et al., 2018; Stuart et al., 2019). However, we noticed there was one cluster of cells with
1222 a much lower number of features in which over 60% of cells had fewer features than the average.
1223 Thus, it was removed from the analysis.

1224 A table of average gene expression for each cluster, and a table of log2 Fold Change values with
1225 p-values between each sample were calculated with Seurat. Seurat calculates differential
1226 expression based on the non-parameteric Wilcoxon rank sum test. Log fold change is calculated
1227 using the average expression between two groups. These values were used in Figure S1 J. and K.
1228 with IPA for a pathway analysis, and in Figure S1 L. to make volcano plots.
1229

1230 **Statistical analysis**

1231 Differences between groups were calculated using the unpaired two-sided Welch's t-test.
1232 Difference between two groups of co-transferred cells, or in bone marrow chimera experiments,
1233 were calculated using the paired two-tailed t-test. Differences between EAE clinical score was
1234 calculated using two-way ANOVA for repeated measures with Bonferroni correction. For RNA-
1235 seq analysis, differential expression was tested by DESeq2 by use of a negative binomial
1236 generalized linear model. We treated less than 0.05 of p value as significant differences. $*p <$
1237 0.05, $**p < 0.01$, $***p < 0.001$, and $****p < 0.0001$. Details regarding number of replicates and
1238 the definition of center/error bars can be found in figure legends.
1239

1240 ## References

1241

1242 Ahern, P.P., Schiering, C., Buonocore, S., McGeachy, M.J., Cua, D.J., Maloy, K.J., and Powrie,
1243 F. (2010). Interleukin-23 Drives Intestinal Inflammation through Direct Activity on T Cells.
1244 Immunity *33*, 279-288.

1245 Awasthi, A., Riol-Blanco, L., Jager, A., Korn, T., Pot, C., Galileos, G., Bettelli, E., Kuchroo,
1246 V.K., and Oukka, M. (2009). Cutting edge: IL-23 receptor gfp reporter mice reveal distinct
1247 populations of IL-17-producing cells. J Immunol *182*, 5904-5908.
1248 Baronciani, L., Zanella, A., Bianchi, P., Zappa, M., Alfinito, F., Iolascon, A., Tannoia, N.,
1249 Beutler, E., and Sirchia, G. (1996). Study of the molecular defects in glucose phosphate
1250 isomerase-deficient patients affected by chronic hemolytic anemia. Blood *88*, 2306-2310.
1251 Becht, E., McInnes, L., Healy, J., Dutertre, C.A., Kwok, I.W.H., Ng, L.G., Ginhoux, F., and
1252 Newell, E.W. (2018). Dimensionality reduction for visualizing single-cell data using UMAP.
1253 Nat Biotechnol.
1254 Bettelli, E., Pagany, M., Weiner, H.L., Linington, C., Sobel, R.A., and Kuchroo, V.K. (2003).
1255 Myelin oligodendrocyte glycoprotein-specific T cell receptor transgenic mice develop
1256 spontaneous autoimmune optic neuritis. J Exp Med *197*, 1073-1081.
1257 Birsoy, K., Wang, T., Chen, W.W., Freinkman, E., Abu-Remaileh, M., and Sabatini, D.M.
1258 (2015). An Essential Role of the Mitochondrial Electron Transport Chain in Cell Proliferation
1259 Is to Enable Aspartate Synthesis. Cell *162*, 540-551.
1260 Bray, N.L., Pimentel, H., Melsted, P., and Pachter, L. (2016). Near-optimal probabilistic RNA-
1261 seq quantification. Nat Biotechnol *34*, 525-527.
1262 Bulcha, J.T., Giese, G.E., Ali, M.Z., Lee, Y.U., Walker, M.D., Holdorf, A.D., Yilmaz, L.S.,
1263 Brewster, R.C., and Walhout, A.J.M. (2019). A Persistence Detector for Metabolic Network
1264 Rewiring in an Animal. Cell Rep *26*, 460-468 e464.
1265 Butler, A., Hoffman, P., Smibert, P., Papalexi, E., and Satija, R. (2018). Integrating single-cell
1266 transcriptomic data across different conditions, technologies, and species. Nat Biotechnol *36*,
1267 411-420.

1268 Corcoran, S.E., and O'Neill, L.A. (2016). HIF1alpha and metabolic reprogramming in
1269 inflammation. J Clin Invest *126*, 3699-3707.
1270 Cua, D.J., Sherlock, J., Chen, Y., Murphy, C.A., Joyce, B., Seymour, B., Lucian, L., To, W.,
1271 Kwan, S., Churakova, T.*, et al.* (2003). Interleukin-23 rather than interleukin-12 is the critical
1272 cytokine for autoimmune inflammation of the brain. Nature *421*, 744-748.
1273 Dang, E.V., Barbi, J., Yang, H.Y., Jinasena, D., Yu, H., Zheng, Y., Bordman, Z., Fu, J., Kim, Y.,
1274 Yen, H.R.*, et al.* (2011). Control of T(H)17/T(reg) balance by hypoxia-inducible factor 1. Cell
1275 *146*, 772-784.
1276 Davies, A.L., Desai, R.A., Bloomfield, P.S., McIntosh, P.R., Chapple, K.J., Linington, C.,
1277 Fairless, R., Diem, R., Kasti, M., Murphy, M.P.*, et al.* (2013). Neurological deficits caused by
1278 tissue hypoxia in neuroinflammatory disease. Ann Neurol *74*, 815-825.
1279 de Padua, M.C., Delodi, G., Vucetic, M., Durivault, J., Vial, V., Bayer, P., Noleto, G.R., Mazure,
1280 N.M., Zdralevic, M., and Pouyssegur, J. (2017). Disrupting glucose-6-phosphate isomerase
1281 fully suppresses the "Warburg effect" and activates OXPHOS with minimal impact on tumor
1282 growth except in hypoxia. Oncotarget *8*, 87623-87637.
1283 Deutscher, D., Meilijson, I., Kupiec, M., and Ruppin, E. (2006). Multiple knockout analysis of
1284 genetic robustness in the yeast metabolic network. Nat Genet *38*, 993-998.
1285 Fernandez, C.A., DesRosiers, C., Previs, S.F., David, F., and Brunengraber, H. (1996).
1286 Correction of C-13 mass isotopomer distributions for natural stable isotope abundance. J Mass
1287 Spectrom *31*, 255-262.
1288 Fotiadou, C., Lazaridou, E., Sotiriou, E., and Ioannides, D. (2018). Targeting IL-23 in psoriasis:
1289 current perspectives. Psoriasis (Auckl) *8*, 1-5.

1290 Ghoreschi, K., Laurence, A., Yang, X.P., Tato, C.M., McGeachy, M.J., Konkel, J.E., Ramos,
1291 H.L., Wei, L., Davidson, T.S., Bouladoux, N., *et al.* (2010). Generation of pathogenic T(H)17
1292 cells in the absence of TGF-beta signalling. Nature *467*, 967-971.
1293 Grassian, A.R., Parker, S.J., Davidson, S.M., Divakaruni, A.S., Green, C.R., Zhang, X., Slocum,
1294 K.L., Pu, M., Lin, F., Vickers, C., *et al.* (2014). IDH1 mutations alter citric acid cycle
1295 metabolism and increase dependence on oxidative mitochondrial metabolism. Cancer Res *74*,
1296 3317-3331.
1297 Hafemeister, C., and Satija, R. (2019). Normalization and variance stabilization of single-cell
1298 RNA-seq data using regularized negative binomial regression. bioRxiv, 576827.
1299 Hanzel, J., and D'Haens, G.R. (2020). Anti-interleukin-23 agents for the treatment of ulcerative
1300 colitis. Expert Opin Biol Ther *20*, 399-406.
1301 Hirota, K., Duarte, J.H., Veldhoen, M., Hornsby, E., Li, Y., Cua, D.J., Ahlfors, H., Wilhelm, C.,
1302 Tolaini, M., Menzel, U., *et al.* (2011). Fate mapping of IL-17-producing T cells in
1303 inflammatory responses. Nat Immunol *12*, 255-263.
1304 Hirota, K., Hashimoto, M., Yoshitomi, H., Tanaka, S., Nomura, T., Yamaguchi, T., Iwakura, Y.,
1305 Sakaguchi, N., and Sakaguchi, S. (2007). T cell self-reactivity forms a cytokine milieu for
1306 spontaneous development of IL-17(+) Th cells that cause autoimmune arthritis. Journal of
1307 Experimental Medicine *204*, 41-47.
1308 Horlbeck, M.A., Xu, A., Wang, M., Bennett, N.K., Park, C.Y., Bogdanoff, D., Adamson, B.,
1309 Chow, E.D., Kampmann, M., Peterson, T.R., *et al.* (2018). Mapping the Genetic Landscape of
1310 Human Cells. Cell *174*, 953-967 e922.

1311 Hue, S., Ahern, P., Buonocore, S., Kullberg, M.C., Cua, D.J., McKenzie, B.S., Powrie, F., and
1312 Maloy, K.J. (2006). Interleukin-23 drives innate and T cell-mediated intestinal inflammation.
1313 J Exp Med *203*, 2473-2483.
1314 Ivanov, II, Atarashi, K., Manel, N., Brodie, E.L., Shima, T., Karaoz, U., Wei, D., Goldfarb, K.C.,
1315 Santee, C.A., Lynch, S.V.*, et al.* (2009). Induction of intestinal Th17 cells by segmented
1316 filamentous bacteria. Cell *139*, 485-498.
1317 Ivanov, II, McKenzie, B.S., Zhou, L., Tadokoro, C.E., Lepelley, A., Lafaille, J.J., Cua, D.J., and
1318 Littman, D.R. (2006). The orphan nuclear receptor RORgammat directs the differentiation
1319 program of proinflammatory IL-17+ T helper cells. Cell *126*, 1121-1133.
1320 Johnson, M.O., Wolf, M.M., Madden, M.Z., Andrejeva, G., Sugiura, A., Contreras, D.C.,
1321 Maseda, D., Liberti, M.V., Paz, K., Kishton, R.J.*, et al.* (2018). Distinct Regulation of Th17
1322 and Th1 Cell Differentiation by Glutaminase-Dependent Metabolism. Cell *175*, 1780-1795
1323 e1719.
1324 Johnson, T.W., Wu, Y., Nathoo, N., Rogers, J.A., Wee Yong, V., and Dunn, J.F. (2016). Gray
1325 Matter Hypoxia in the Brain of the Experimental Autoimmune Encephalomyelitis Model of
1326 Multiple Sclerosis. PLoS One *11*, e0167196.
1327 Kanno, H., Fujii, H., Hirono, A., Ishida, Y., Ohga, S., Fukumoto, Y., Matsuzawa, K., Ogawa, S.,
1328 and Miwa, S. (1996). Molecular analysis of glucose phosphate isomerase deficiency
1329 associated with hereditary hemolytic anemia. Blood *88*, 2321-2325.
1330 Karhausen, J., Furuta, G.T., Tomaszewski, J.E., Johnson, R.S., Colgan, S.P., and Haase, V.H.
1331 (2004). Epithelial hypoxia-inducible factor-1 is protective in murine experimental colitis. J
1332 Clin Invest *114*, 1098-1106.

1333 Kugler, W., Breme, K., Laspe, P., Muirhead, H., Davies, C., Winkler, H., Schroter, W., and
1334 Lakomek, M. (1998). Molecular basis of neurological dysfunction coupled with haemolytic
1335 anaemia in human glucose-6-phosphate isomerase (GPI) deficiency. Hum Genet *103*, 450-
1336 454.
1337 Kullberg, M.C., Jankovic, D., Feng, C.G., Hue, S., Gorelick, P.L., McKenzie, B.S., Cua, D.J.,
1338 Powrie, F., Cheever, A.W., Maloy, K.J.*, et al.* (2006). IL-23 plays a key role in Helicobacter
1339 hepaticus-induced T cell-dependent colitis. J Exp Med *203*, 2485-2494.
1340 Kumar, P., Monin, L., Castillo, P., Elsegeiny, W., Horne, W., Eddens, T., Vikram, A., Good, M.,
1341 Schoenborn, A.A., Bibby, K.*, et al.* (2016). Intestinal Interleukin-17 Receptor Signaling
1342 Mediates Reciprocal Control of the Gut Microbiota and Autoimmune Inflammation.
1343 Immunity *44*, 659-671.
1344 Langley, R.G., Tsai, T.F., Flavin, S., Song, M., Randazzo, B., Wasfi, Y., Jiang, J., Li, S., and
1345 Puig, L. (2018). Efficacy and safety of guselkumab in patients with psoriasis who have an
1346 inadequate response to ustekinumab: results of the randomized, double-blind, phase III
1347 NAVIGATE trial. Br J Dermatol *178*, 114-123.
1348 Lee, P., Chandel, N.S., and Simon, M.C. (2020). Cellular adaptation to hypoxia through hypoxia
1349 inducible factors and beyond. Nat Rev Mol Cell Biol.
1350 Lee, W.N., Boros, L.G., Puigjaner, J., Bassilian, S., Lim, S., and Cascante, M. (1998). Mass
1351 isotopomer study of the nonoxidative pathways of the pentose cycle with [1,2-13C2]glucose.
1352 Am J Physiol *274*, E843-851.
1353 Lewis, C.A., Parker, S.J., Fiske, B.P., McCloskey, D., Gui, D.Y., Green, C.R., Vokes, N.I., Feist,
1354 A.M., Vander Heiden, M.G., and Metallo, C.M. (2014). Tracing compartmentalized NADPH
1355 metabolism in the cytosol and mitochondria of mammalian cells. Mol Cell *55*, 253-263.

1356 Li, Z.H., Dulyaninova, N.G., House, R.P., Almo, S.C., and Bresnick, A.R. (2010). S100A4
1357 regulates macrophage chemotaxis. Mol Biol Cell *21*, 2598-2610.
1358 Liberti, M.V., Dai, Z.W., Wardell, S.E., Baccile, J.A., Liu, X.J., Gao, X., Baldi, R.,
1359 Mehrmohamadi, M., Johnson, M.O., Madhukar, N.S.*, et al.* (2017). A Predictive Model for
1360 Selective Targeting of the Warburg Effect through GAPDH Inhibition with a Natural Product.
1361 Cell Metab *26*, 648-+.
1362 Ma, E.H., Verway, M.J., Johnson, R.M., Roy, D.G., Steadman, M., Hayes, S., Williams, K.S.,
1363 Sheldon, R.D., Samborska, B., Kosinski, P.A.*, et al.* (2019). Metabolic Profiling Using Stable
1364 Isotope Tracing Reveals Distinct Patterns of Glucose Utilization by Physiologically Activated
1365 CD8(+) T Cells. Immunity *51*, 856-870 e855.
1366 Macintyre, A.N., Gerriets, V.A., Nichols, A.G., Michalek, R.D., Rudolph, M.C., Deoliveira, D.,
1367 Anderson, S.M., Abel, E.D., Chen, B.J., Hale, L.P.*, et al.* (2014). The glucose transporter
1368 Glut1 is selectively essential for CD4 T cell activation and effector function. Cell Metab *20*,
1369 61-72.
1370 MacIver, N.J., Michalek, R.D., and Rathmell, J.C. (2013). Metabolic regulation of T
1371 lymphocytes. Annu Rev Immunol *31*, 259-283.
1372 Mao, K., Baptista, A.P., Tamoutounour, S., Zhuang, L., Bouladoux, N., Martins, A.J., Huang, Y.,
1373 Gerner, M.Y., Belkaid, Y., and Germain, R.N. (2018). Innate and adaptive lymphocytes
1374 sequentially shape the gut microbiota and lipid metabolism. Nature *554*, 255-259.
1375 McGeachy, M.J., Chen, Y., Tato, C.M., Laurence, A., Joyce-Shaikh, B., Blumenschein, W.M.,
1376 McClanahan, T.K., O'Shea, J.J., and Cua, D.J. (2009). The interleukin 23 receptor is essential
1377 for the terminal differentiation of interleukin 17-producing effector T helper cells in vivo. Nat
1378 Immunol *10*, 314-324.

1379 McInnes, L., and Healy, J. (2018). UMAP: Uniform Manifold Approximation and Projection for
1380 Dimension Reduction. ArXiv *abs/1802.03426*.
1381 McMullin, M.F. (1999). The molecular basis of disorders of red cell enzymes. J Clin Pathol *52*,
1382 241-244.
1383 Metallo, C.M., Gameiro, P.A., Bell, E.L., Mattaini, K.R., Yang, J., Hiller, K., Jewell, C.M.,
1384 Johnson, Z.R., Irvine, D.J., Guarente, L.*, et al.* (2011). Reductive glutamine metabolism by
1385 IDH1 mediates lipogenesis under hypoxia. Nature *481*, 380-384.
1386 Michalek, R.D., Gerriets, V.A., Jacobs, S.R., Macintyre, A.N., MacIver, N.J., Mason, E.F.,
1387 Sullivan, S.A., Nichols, A.G., and Rathmell, J.C. (2011). Cutting edge: distinct glycolytic and
1388 lipid oxidative metabolic programs are essential for effector and regulatory CD4+ T cell
1389 subsets. J Immunol *186*, 3299-3303.
1390 Milner, J.D., and Holland, S.M. (2013). The cup runneth over: lessons from the ever-expanding
1391 pool of primary immunodeficiency diseases. Nat Rev Immunol *13*, 635-648.
1392 Morrison, P.J., Bending, D., Fouser, L.A., Wright, J.F., Stockinger, B., Cooke, A., and Kullberg,
1393 M.C. (2013). Th17-cell plasticity in Helicobacter hepaticus-induced intestinal inflammation.
1394 Mucosal Immunol *6*, 1143-1156.
1395 Moschen, A.R., Tilg, H., and Raine, T. (2019). IL-12, IL-23 and IL-17 in IBD: immunobiology
1396 and therapeutic targeting. Nat Rev Gastroenterol Hepatol *16*, 185-196.
1397 Murphy, C.A., Langrish, C.L., Chen, Y., Blumenschein, W., McClanahan, T., Kastelein, R.A.,
1398 Sedgwick, J.D., and Cua, D.J. (2003). Divergent pro- and antiinflammatory roles for IL-23
1399 and IL-12 in joint autoimmune inflammation. J Exp Med *198*, 1951-1957.
1400 Nakae, S., Nambu, A., Sudo, K., and Iwakura, Y. (2003a). Suppression of immune induction of
1401 collagen-induced arthritis in IL-17-deficient mice. J Immunol *171*, 6173-6177.

1402 Nakae, S., Saijo, S., Horai, R., Sudo, K., Mori, S., and Iwakura, Y. (2003b). IL-17 production
1403 from activated T cells is required for the spontaneous development of destructive arthritis in
1404 mice deficient in IL-1 receptor antagonist. P Natl Acad Sci USA *100*, 5986-5990.
1405 Naughton, D.P., Haywood, R., Blake, D.R., Edmonds, S., Hawkes, G.E., and Grootveld, M.
1406 (1993). A comparative evaluation of the metabolic profiles of normal and inflammatory knee-
1407 joint synovial fluids by high resolution proton NMR spectroscopy. FEBS Lett *332*, 221-225.
1408 Ng, C., Aichinger, M., Nguyen, T., Au, C., Najar, T., Wu, L., Mesa, K.R., Liao, W., Quivy, J.P.,
1409 Hubert, B.*, et al.* (2019). The histone chaperone CAF-1 cooperates with the DNA
1410 methyltransferases to maintain Cd4 silencing in cytotoxic T cells. Genes Dev *33*, 669-683.
1411 Ng, C.T., Biniecka, M., Kennedy, A., McCormick, J., Fitzgerald, O., Bresnihan, B., Buggy, D.,
1412 Taylor, C.T., O'Sullivan, J., Fearon, U.*, et al.* (2010). Synovial tissue hypoxia and
1413 inflammation in vivo. Ann Rheum Dis *69*, 1389-1395.
1414 O'Neill, L.A., Kishton, R.J., and Rathmell, J. (2016). A guide to immunometabolism for
1415 immunologists. Nat Rev Immunol *16*, 553-565.
1416 Okada, S., Markle, J.G., Deenick, E.K., Mele, F., Averbuch, D., Lagos, M., Alzahrani, M., Al-
1417 Muhsen, S., Halwani, R., Ma, C.S.*, et al.* (2015). IMMUNODEFICIENCIES. Impairment of
1418 immunity to Candida and Mycobacterium in humans with bi-allelic RORC mutations. Science
1419 *349*, 606-613.
1420 Olenchock, B.A., Rathmell, J.C., and Vander Heiden, M.G. (2017). Biochemical Underpinnings
1421 of Immune Cell Metabolic Phenotypes. Immunity *46*, 703-713.
1422 Omenetti, S., Bussi, C., Metidji, A., Iseppon, A., Lee, S., Tolaini, M., Li, Y., Kelly, G.,
1423 Chakravarty, P., Shoaie, S.*, et al.* (2019). The Intestine Harbors Functionally Distinct
1424 Homeostatic Tissue-Resident and Inflammatory Th17 Cells. Immunity *51*, 77-89 e76.

1425 Pacold, M.E., Brimacombe, K.R., Chan, S.H., Rohde, J.M., Lewis, C.A., Swier, L.J., Possemato,
1426 R., Chen, W.W., Sullivan, L.B., Fiske, B.P., *et al.* (2016). A PHGDH inhibitor reveals
1427 coordination of serine synthesis and one-carbon unit fate. Nat Chem Biol *12*, 452-458.
1428 Pariser, D., Frankel, E., Schlessinger, J., Poulin, Y., Vender, R., Langley, R.G., Meng, X.,
1429 Guana, A., and Nyirady, J. (2018). Efficacy of Secukinumab in the Treatment of Moderate to
1430 Severe Plaque Psoriasis in the North American Subgroup of Patients: Pooled Analysis of Four
1431 Phase 3 Studies. Dermatol Ther (Heidelb) *8*, 17-32.
1432 Peng, M., Yin, N., Chhangawala, S., Xu, K., Leslie, C.S., and Li, M.O. (2016). Aerobic
1433 glycolysis promotes T helper 1 cell differentiation through an epigenetic mechanism. Science
1434 *354*, 481-484.
1435 Peters, C.L., Morris, C.J., Mapp, P.I., Blake, D.R., Lewis, C.E., and Winrow, V.R. (2004). The
1436 transcription factors hypoxia-inducible factor 1alpha and Ets-1 colocalize in the hypoxic
1437 synovium of inflamed joints in adjuvant-induced arthritis. Arthritis Rheum *50*, 291-296.
1438 Picelli, S., Faridani, O.R., Bjorklund, A.K., Winberg, G., Sagasser, S., and Sandberg, R. (2014).
1439 Full-length RNA-seq from single cells using Smart-seq2. Nat Protoc *9*, 171-181.
1440 Piskin, G., Sylva-Steenland, R.M., Bos, J.D., and Teunissen, M.B. (2006). In vitro and in situ
1441 expression of IL-23 by keratinocytes in healthy skin and psoriasis lesions: enhanced
1442 expression in psoriatic skin. J Immunol *176*, 1908-1915.
1443 Platt, R.J., Chen, S., Zhou, Y., Yim, M.J., Swiech, L., Kempton, H.R., Dahlman, J.E., Parnas, O.,
1444 Eisenhaure, T.M., Jovanovic, M., *et al.* (2014). CRISPR-Cas9 knockin mice for genome
1445 editing and cancer modeling. Cell *159*, 440-455.

1446 Puel, A., Cypowyj, S., Bustamante, J., Wright, J.F., Liu, L., Lim, H.K., Migaud, M., Israel, L.,
1447 Chrabieh, M., Audry, M., *et al.* (2011). Chronic mucocutaneous candidiasis in humans with
1448 inborn errors of interleukin-17 immunity. Science *332*, 65-68.
1449 Raez, L.E., Papadopoulos, K., Ricart, A.D., Chiorean, E.G., Dipaola, R.S., Stein, M.N., Rocha
1450 Lima, C.M., Schlesselman, J.J., Tolba, K., Langmuir, V.K., *et al.* (2013). A phase I dose-
1451 escalation trial of 2-deoxy-D-glucose alone or combined with docetaxel in patients with
1452 advanced solid tumors. Cancer Chemother Pharmacol *71*, 523-530.
1453 Schneider, A.S. (2000). Triosephosphate isomerase deficiency: historical perspectives and
1454 molecular aspects. Best Pract Res Cl Ha *13*, 119-140.
1455 Segre, D., Deluna, A., Church, G.M., and Kishony, R. (2005). Modular epistasis in yeast
1456 metabolism. Nat Genet *37*, 77-83.
1457 Semenza, G.L. (2013). HIF-1 mediates metabolic responses to intratumoral hypoxia and
1458 oncogenic mutations. J Clin Invest *123*, 3664-3671.
1459 Semenza, G.L. (2014). Oxygen sensing, hypoxia-inducible factors, and disease pathophysiology.
1460 Annu Rev Pathol *9*, 47-71.
1461 Shi, L.Z., Wang, R., Huang, G., Vogel, P., Neale, G., Green, D.R., and Chi, H. (2011).
1462 HIF1alpha-dependent glycolytic pathway orchestrates a metabolic checkpoint for the
1463 differentiation of TH17 and Treg cells. J Exp Med *208*, 1367-1376.
1464 Stuart, T., Butler, A., Hoffman, P., Hafemeister, C., Papalexi, E., Mauck, W.M., 3rd, Hao, Y.,
1465 Stoeckius, M., Smibert, P., and Satija, R. (2019). Comprehensive Integration of Single-Cell
1466 Data. Cell *177*, 1888-1902 e1821.

1467 Sullivan, L.B., Gui, D.Y., Hosios, A.M., Bush, L.N., Freinkman, E., and Vander Heiden, M.G.
1468 (2015). Supporting Aspartate Biosynthesis Is an Essential Function of Respiration in
1469 Proliferating Cells. Cell *162*, 552-563.
1470 Tahir, H. (2018). Therapies in ankylosing spondylitis-from clinical trials to clinical practice.
1471 Rheumatology (Oxford) *57*, vi23-vi28.
1472 Thiele, I., Vo, T.D., Price, N.D., and Palsson, B.O. (2005). Expanded metabolic reconstruction of
1473 Helicobacter pylori (iIT341 GSM/GPR): an in silico genome-scale characterization of single-
1474 and double-deletion mutants. J Bacteriol *187*, 5818-5830.
1475 Van Welden, S., Selfridge, A.C., and Hindryckx, P. (2017). Intestinal hypoxia and hypoxia-
1476 induced signalling as therapeutic targets for IBD. Nat Rev Gastroenterol Hepatol *14*, 596-611.
1477 Vander Heiden, M.G., Cantley, L.C., and Thompson, C.B. (2009). Understanding the Warburg
1478 effect: the metabolic requirements of cell proliferation. Science *324*, 1029-1033.
1479 Vander Heiden, M.G., and DeBerardinis, R.J. (2017). Understanding the Intersections between
1480 Metabolism and Cancer Biology. Cell *168*, 657-669.
1481 Veldhoen, M., Hocking, R.J., Atkins, C.J., Locksley, R.M., and Stockinger, B. (2006). TGFbeta
1482 in the context of an inflammatory cytokine milieu supports de novo differentiation of IL-17-
1483 producing T cells. Immunity *24*, 179-189.
1484 Wang, E.A., Suzuki, E., Maverakis, E., and Adamopoulos, I.E. (2017). Targeting IL-17 in
1485 psoriatic arthritis. Eur J Rheumatol *4*, 272-277.
1486 Warburg, O., Gawehn, K., and Geissler, A.W. (1958). [Metabolism of leukocytes]. Z
1487 Naturforsch B *13B*, 515-516.

1488 Xu, M., Pokrovskii, M., Ding, Y., Yi, R., Au, C., Harrison, O.J., Galan, C., Belkaid, Y.,
1489 Bonneau, R., and Littman, D.R. (2018). c-MAF-dependent regulatory T cells mediate
1490 immunological tolerance to a gut pathobiont. Nature *554*, 373-377.
1491 Yang, R., and Dunn, J.F. (2015). Reduced cortical microvascular oxygenation in multiple
1492 sclerosis: a blinded, case-controlled study using a novel quantitative near-infrared
1493 spectroscopy method. Sci Rep *5*, 16477.
1494 Yang, Y., Torchinsky, M.B., Gobert, M., Xiong, H., Xu, M., Linehan, J.L., Alonzo, F., Ng, C.,
1495 Chen, A., Lin, X.*, et al.* (2014). Focused specificity of intestinal TH17 cells towards
1496 commensal bacterial antigens. Nature *510*, 152-156.
1497 Yuan, J., Bennett, B.D., and Rabinowitz, J.D. (2008). Kinetic flux profiling for quantitation of
1498 cellular metabolic fluxes. Nat Protoc *3*, 1328-1340.
1499 Zaidi, A.U., Kedar, P., Koduri, P.R., Goyette, G.W., Buck, S., Paglia, D.E., and Ravindranath, Y.
1500 (2017). Glucose phosphate isomerase (GPI) Tadikonda: Characterization of a novel
1501 Pro340Ser mutation. Pediatr Hemat Oncol *34*, 449-454.
1502 Zanella, A., Fermo, E., Bianchi, P., and Valentini, G. (2005). Red cell pyruvate kinase
1503 deficiency: molecular and clinical aspects. Br J Haematol *130*, 11-25.
1504 Zhao, D., Badur, M.G., Luebeck, J., Magana, J.H., Birmingham, A., Sasik, R., Ahn, C.S., Ideker,
1505 T., Metallo, C.M., and Mali, P. (2018). Combinatorial CRISPR-Cas9 Metabolic Screens
1506 Reveal Critical Redox Control Points Dependent on the KEAP1-NRF2 Regulatory Axis. Mol
1507 Cell *69*, 699-708 e697.
1508 Zheng, Y., Danilenko, D.M., Valdez, P., Kasman, I., Eastham-Anderson, J., Wu, J., and Ouyang,
1509 W. (2007). Interleukin-22, a T(H)17 cytokine, mediates IL-23-induced dermal inflammation
1510 and acanthosis. Nature *445*, 648-651.

1511 Zhu, J., and Thompson, C.B. (2019). Metabolic regulation of cell growth and proliferation. Nat
1512 Rev Mol Cell Biol *20*, 436-450.
1513

Figure 1

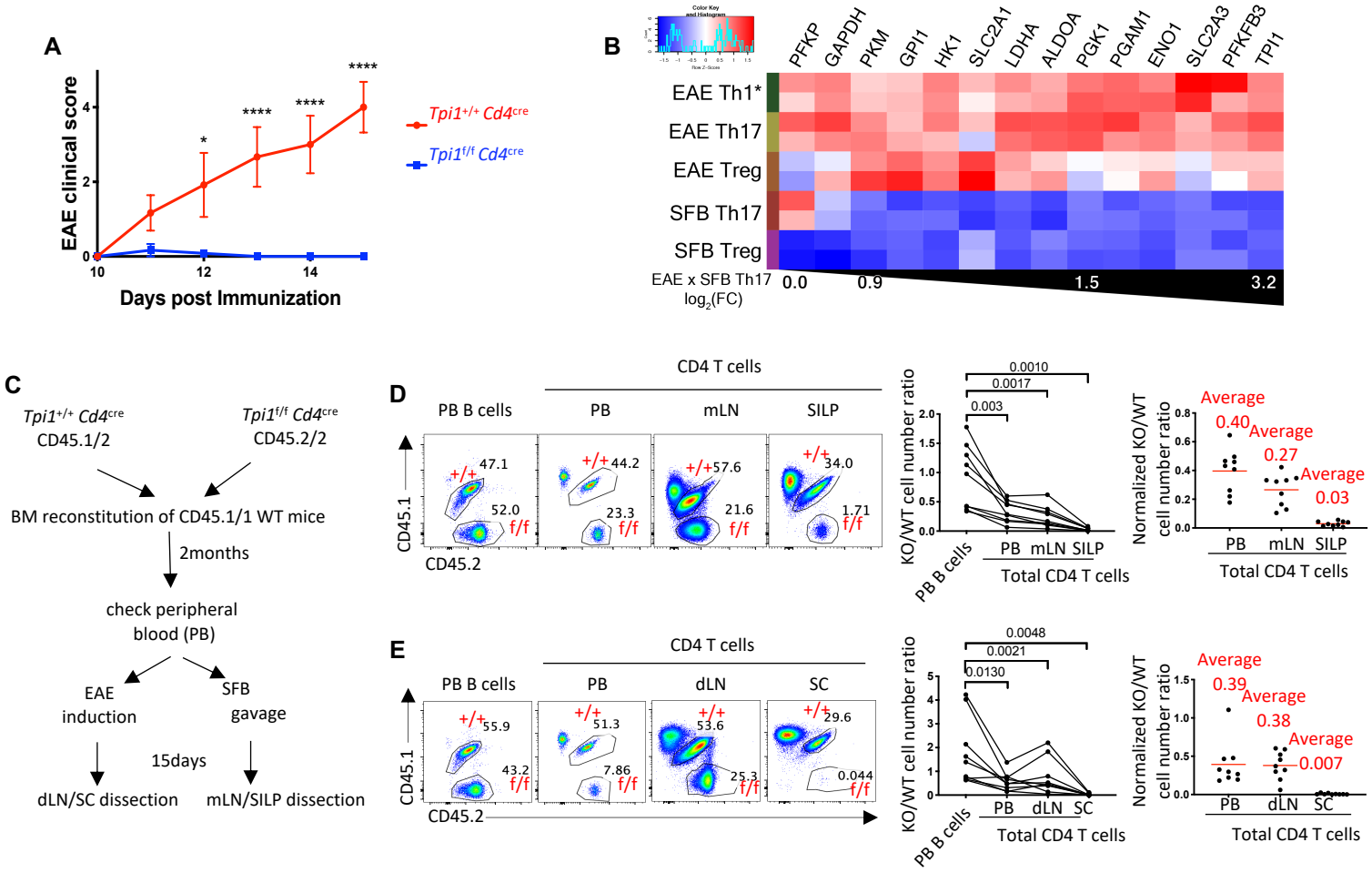
A
EAE clinical score
Days post Immunization
Tpi1+/+ Cd4cre
Tpi1f/f Cd4cre
B
PFKP
GAPDH
PKM
GPI1
HK1
SLC2A1
LDHA
ALDOA
PGK1
PGAM1
ENO1
SLC2A3
PFKFB3
TPI1
EAE Th1*
EAE Th17
EAE Treg
SFB Th17
SFB Treg
EAE x SFB Th17
log2(FC)
0.0
0.9
1.5
3.2
C
Tpi1+/+ Cd4cre
CD45.1/2
Tpi1f/f Cd4cre
CD45.2/2
BM reconstitution of CD45.1/1 WT mice
2months
check peripheral blood (PB)
EAE induction
SFB gavage
15days
dLN/SC dissection
mLN/SILP dissection
D
CD4 T cells
PB B cells
PB
mLN
SILP
CD45.1
CD45.2
KO/WT cell number ratio
Total CD4 T cells
Normalized KO/WT cell number ratio
Average 0.40
Average 0.27
Average 0.03
E
CD4 T cells
PB B cells
PB
dLN
SC
Average 0.39
Average 0.38
Average 0.007

Figure 2

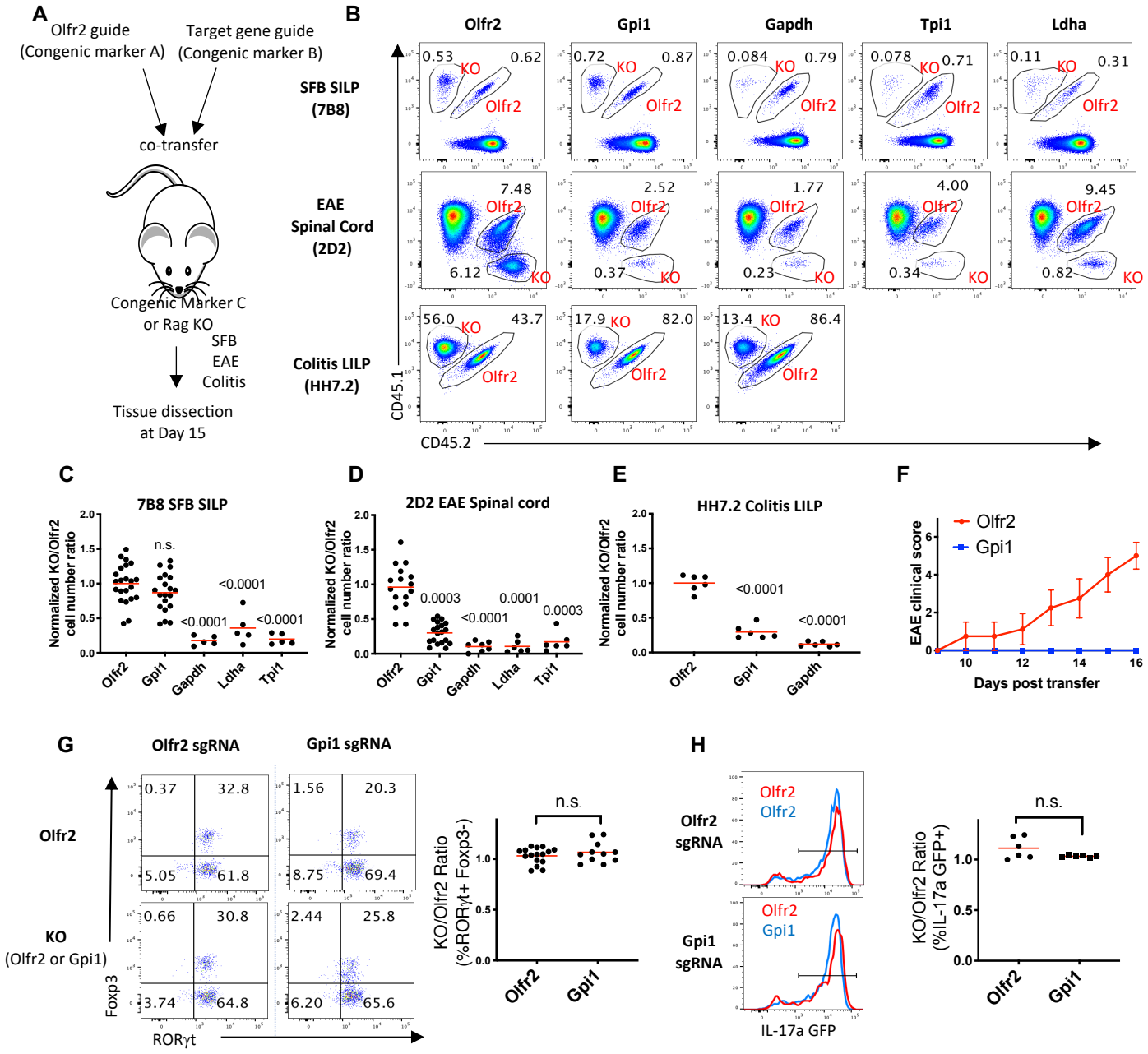
A
Olfr2 guide
(Congenic marker A)
Target gene guide
(Congenic marker B)
co-transfer
Congenic Marker C
or Rag KO
SFB
EAE
Colitis
Tissue dissection
at Day 15
B
Olfr2
Gpi1
Gapdh
Tpi1
Ldha
SFB SILP
(7B8)
EAE
Spinal Cord
(2D2)
Colitis LILP
(HH7.2)
CD45.1
CD45.2
KO
Olfr2
C
7B8 SFB SILP
Normalized KO/Olfr2 cell number ratio
n.s.
<0.0001
D
2D2 EAE Spinal cord
0.0003
0.0001
E
HH7.2 Colitis LILP
F
EAE clinical score
Days post transfer
G
Olfr2 sgRNA
Gpi1 sgRNA
KO
(Olfr2 or Gpi1)
Foxp3
RORγt
KO/Olfr2 Ratio
(%RORγt+ Foxp3-)
H
Olfr2
sgRNA
Gpi1
sgRNA
IL-17a GFP
KO/Olfr2 Ratio
(%IL-17a GFP+)

Figure 3

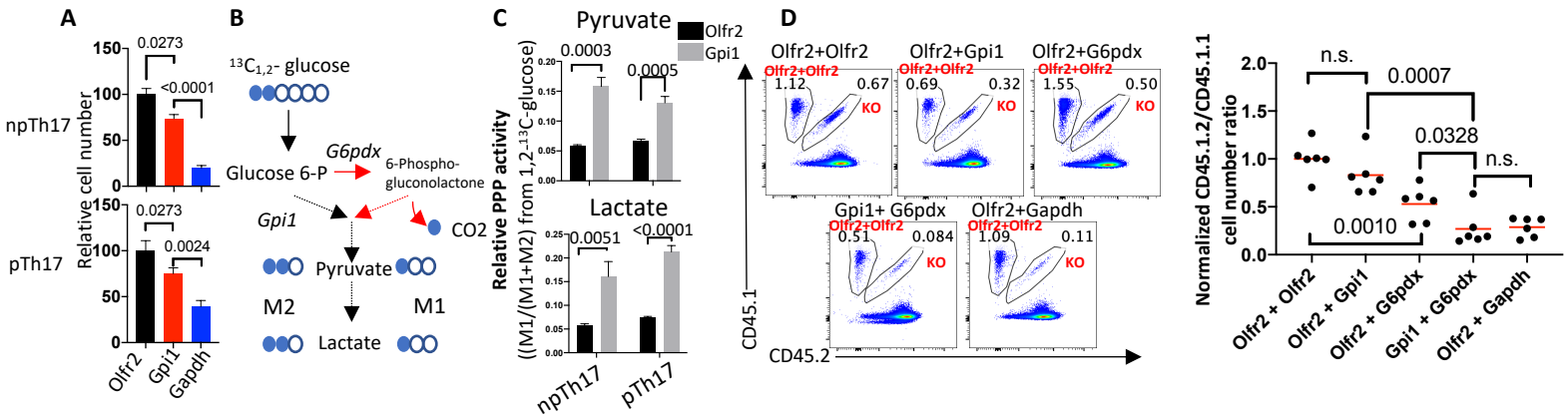
A
B
C
D
Relative cell number
npTh17
pTh17
0.0273
<0.0001
0.0273
0.0024
Olfr2
Gpi1
Gapdh
13C1,2- glucose
Glucose 6-P
G6pdx
6-Phospho-gluconolactone
Gpi1
CO2
Pyruvate
M2
M1
Lactate
Pyruvate
Lactate
Olfr2
Gpi1
Relative PPP activity
((M1/(M1+M2) from 1,2-13C-glucose)
0.0003
0.0005
0.0051
<0.0001
npTh17
pTh17
Olfr2+Olfr2
Olfr2+Gpi1
Olfr2+G6pdx
Gpi1+ G6pdx
Olfr2+Gapdh
1.12
0.67
0.69
0.32
1.55
0.50
0.51
0.084
1.09
0.11
KO
CD45.1
CD45.2
Normalized CD45.1.2/CD45.1.1 cell number ratio
n.s.
0.0007
0.0328
n.s.
0.0010
Olfr2 + Olfr2
Olfr2 + Gpi1
Olfr2 + G6pdx
Gpi1 + G6pdx
Olfr2 + Gapdh

Figure 4

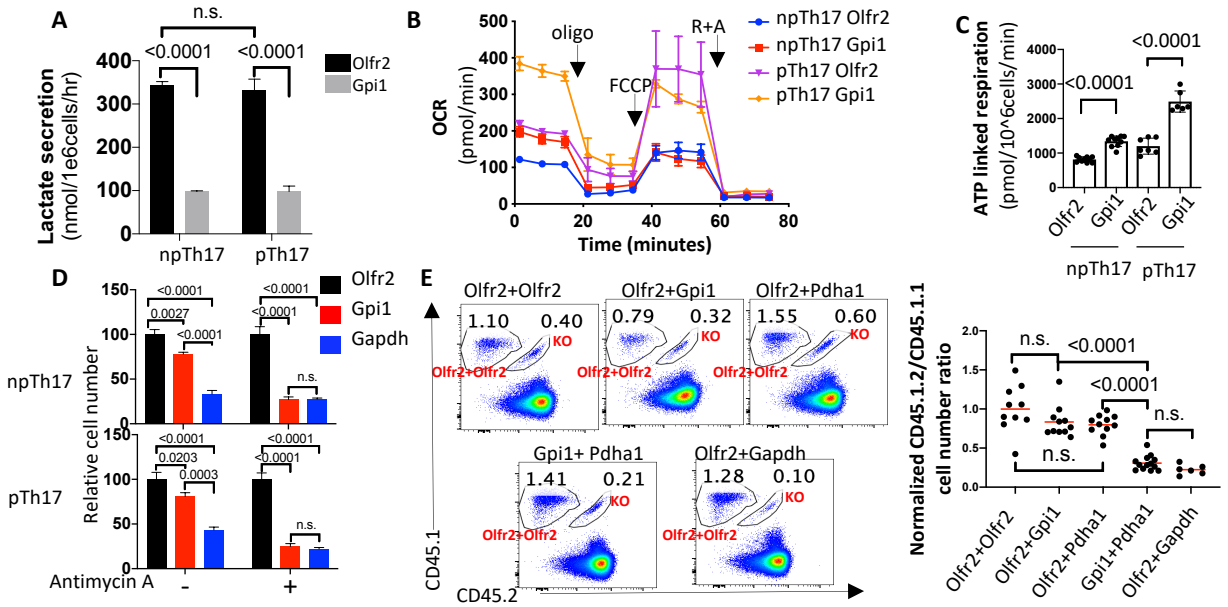
A
n.s.
<0.0001
<0.0001
Lactate secretion (nmol/1e6cells/hr)
Olfr2
Gpi1
npTh17
pTh17
B
oligo
FCCP
R+A
OCR (pmol/min)
Time (minutes)
npTh17 Olfr2
npTh17 Gpi1
pTh17 Olfr2
pTh17 Gpi1
C
ATP linked respiration (pmol/10^6cells/min)
<0.0001
<0.0001
Olfr2
Gpi1
Olfr2
Gpi1
npTh17
pTh17
D
Olfr2
Gpi1
Gapdh
Relative cell number
npTh17
pTh17
Antimycin A
-
+
E
Olfr2+Olfr2
Olfr2+Gpi1
Olfr2+Pdha1
Gpi1+ Pdha1
Olfr2+Gapdh
1.10
0.40
0.79
0.32
1.55
0.60
1.41
0.21
1.28
0.10
KO
CD45.1
CD45.2
Normalized CD45.1.2/CD45.1.1 cell number ratio
n.s.
<0.0001
<0.0001
n.s.
n.s.
Olfr2+Olfr2
Olfr2+Gpi1
Olfr2+Pdha1
Gpi1+Pdha1
Olfr2+Gapdh

Figure 5

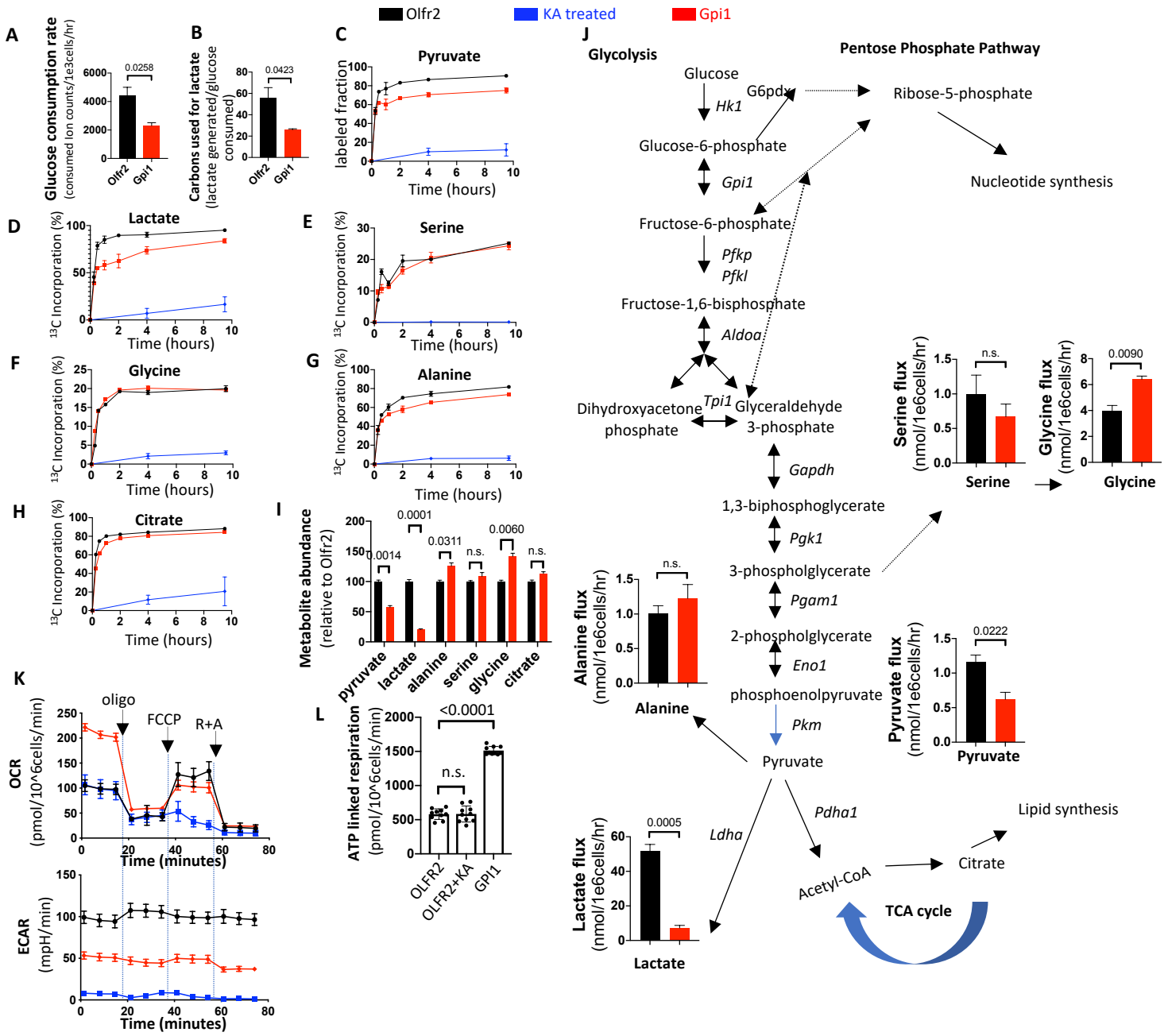
Olfr2
KA treated
Gpi1
A
Glucose consumption rate
(consumed Ion counts/1e3cells/hr)
0.0258
Olfr2
Gpi1
B
Carbons used for lactate
(lactate generated/glucose consumed)
0.0423
C
Pyruvate
labeled fraction
Time (hours)
D
Lactate
E
Serine
F
Glycine
G
Alanine
H
Citrate
13C Incorporation (%)
I
Metabolite abundance
(relative to Olfr2)
0.0014
0.0001
0.0311
n.s.
0.0060
n.s.
pyruvate
lactate
alanine
serine
glycine
citrate
J
Glycolysis
Pentose Phosphate Pathway
Glucose
G6pdx
Hk1
Ribose-5-phosphate
Glucose-6-phosphate
Nucleotide synthesis
Gpi1
Fructose-6-phosphate
Pfkp
Pfkl
Fructose-1,6-bisphosphate
Aldoa
Dihydroxyacetone phosphate
Tpi1
Glyceraldehyde 3-phosphate
Gapdh
1,3-biphosphoglycerate
Pgk1
3-phospholglycerate
Pgam1
2-phospholglycerate
Eno1
phosphoenolpyruvate
Pkm
Pyruvate
Ldha
Pdha1
Acetyl-CoA
Citrate
Lipid synthesis
TCA cycle
Serine flux
(nmol/1e6cells/hr)
n.s.
Serine
Glycine flux
(nmol/1e6cells/hr)
0.0090
Glycine
Alanine flux
(nmol/1e6cells/hr)
n.s.
Alanine
Pyruvate flux
(nmol/1e6cells/hr)
0.0222
Pyruvate
Lactate flux
(nmol/1e6cells/hr)
0.0005
Lactate
K
OCR
(pmol/10^6cells/min)
oligo
FCCP
R+A
Time (minutes)
ECAR
(mpH/min)
Time (minutes)
L
ATP linked respiration
(pmol/10^6cells/min)
<0.0001
n.s.
OLFR2
OLFR2+KA
GPI1

Figure 6

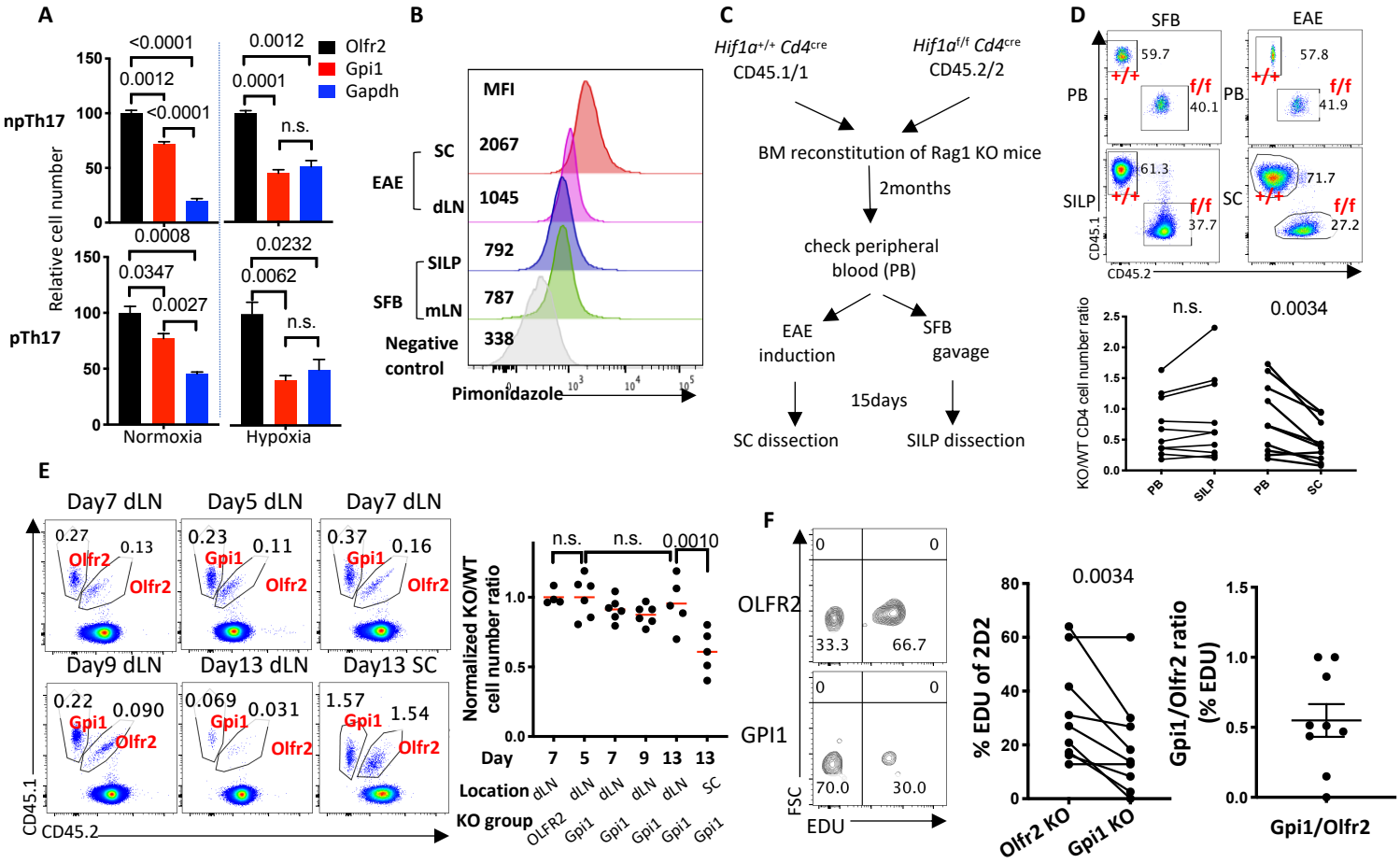
A
Olfr2
Gpi1
Gapdh
npTh17
pTh17
Relative cell number
Normoxia
Hypoxia
<0.0001
0.0012
0.0001
n.s.
0.0008
0.0347
0.0027
0.0232
0.0062
B
MFI
SC
EAE
dLN
SILP
SFB
mLN
Negative control
2067
1045
792
787
338
Pimonidazole
C
Hif1a+/+ Cd4cre
CD45.1/1
Hif1af/f Cd4cre
CD45.2/2
BM reconstitution of Rag1 KO mice
2months
check peripheral blood (PB)
EAE induction
SFB gavage
15days
SC dissection
SILP dissection
D
SFB
EAE
PB
SILP
SC
+/+
f/f
59.7
40.1
61.3
37.7
57.8
41.9
71.7
27.2
CD45.1
CD45.2
KO/WT CD4 cell number ratio
n.s.
0.0034
E
Day7 dLN
Day5 dLN
Day7 dLN
Day9 dLN
Day13 dLN
Day13 SC
Olfr2
Gpi1
0.27
0.13
0.23
0.11
0.37
0.16
0.22
0.090
0.069
0.031
1.57
1.54
CD45.1
CD45.2
Normalized KO/WT cell number ratio
n.s.
n.s.
0.0010
Day
Location
KO group
F
OLFR2
GPI1
FSC
EDU
33.3
66.7
70.0
30.0
% EDU of 2D2
0.0034
Olfr2 KO
Gpi1 KO
Gpi1/Olfr2 ratio (% EDU)
Gpi1/Olfr2

Supplementary figure 1

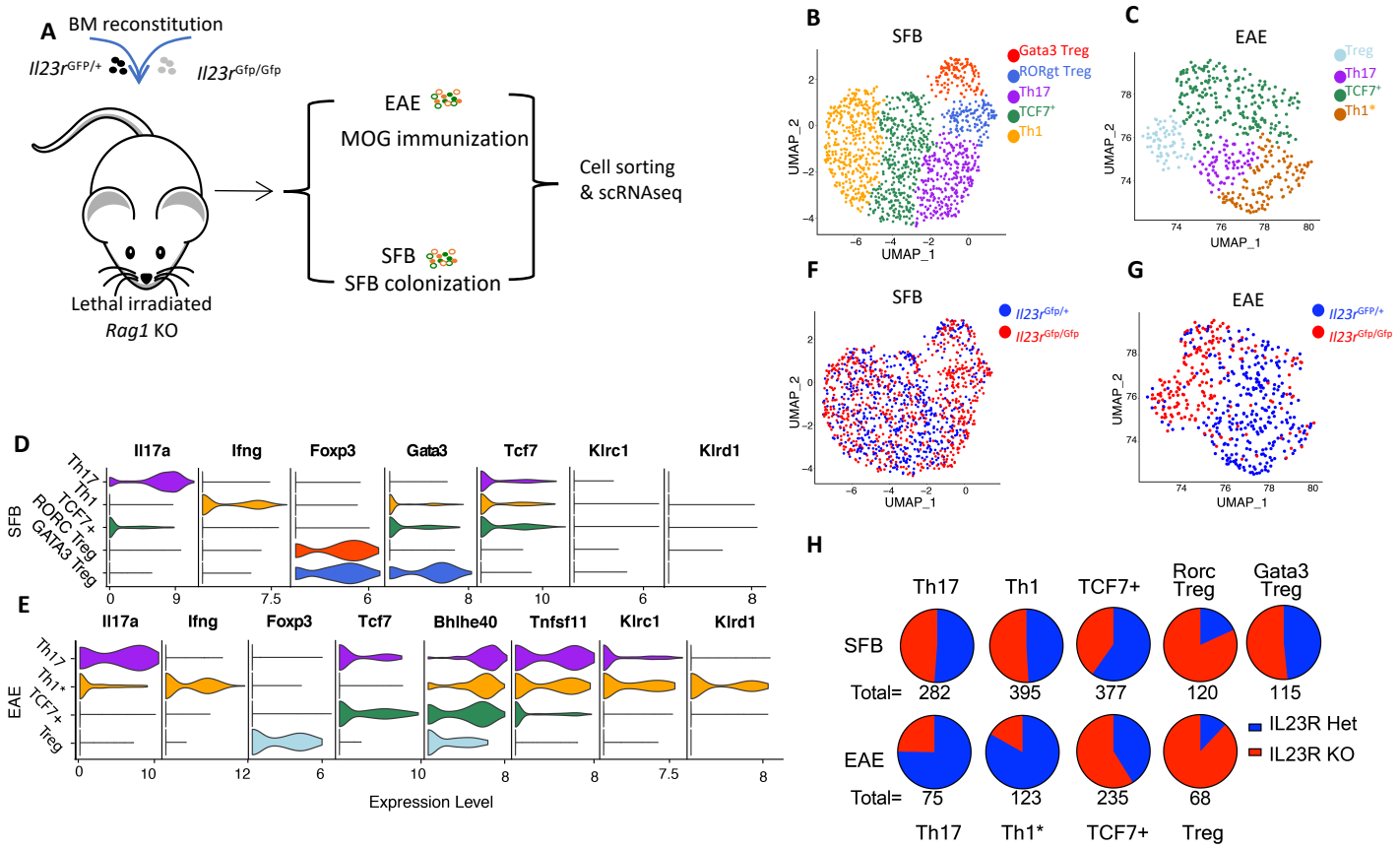

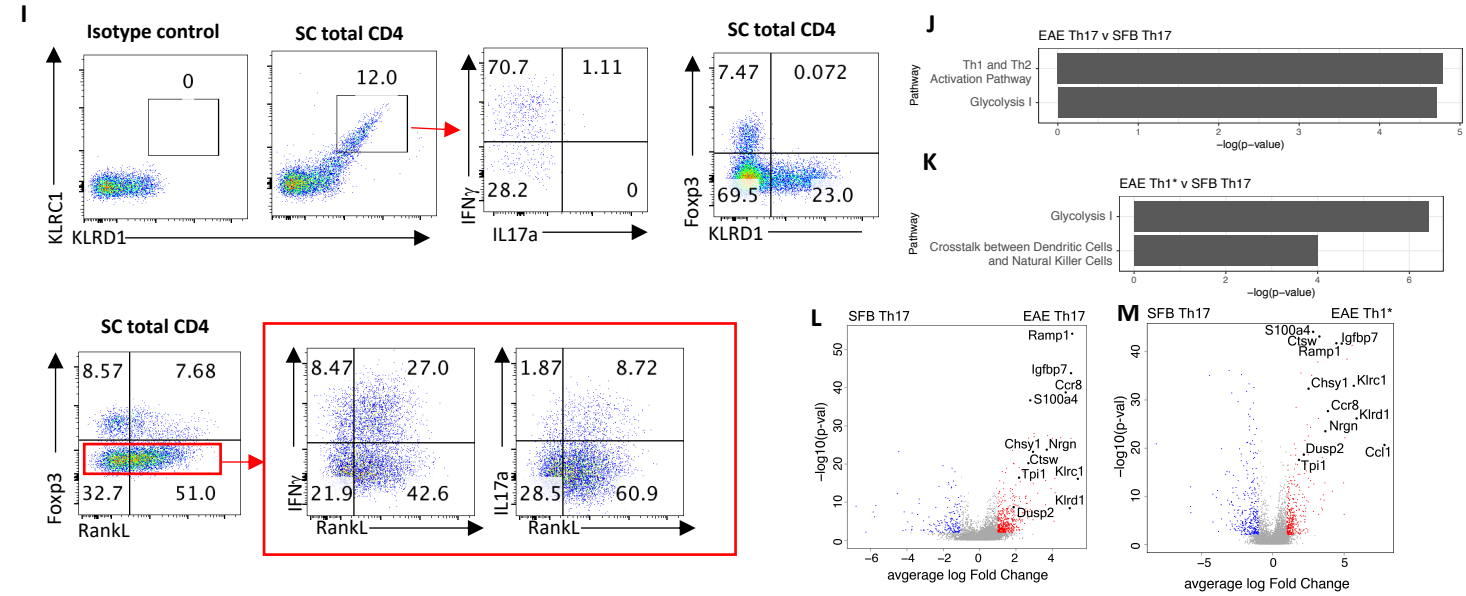

Supplementary figure 2

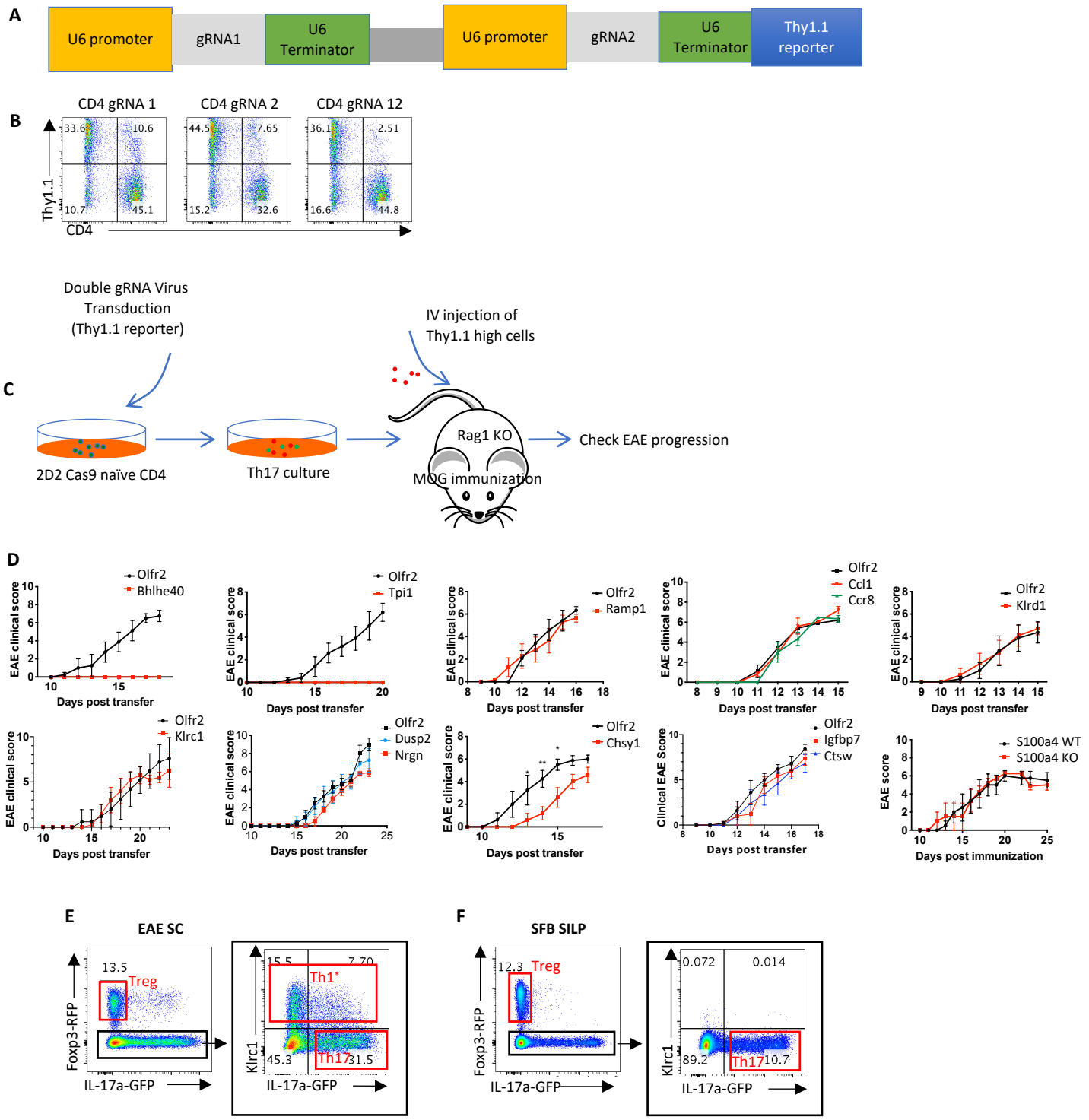

Supplementary figure 3

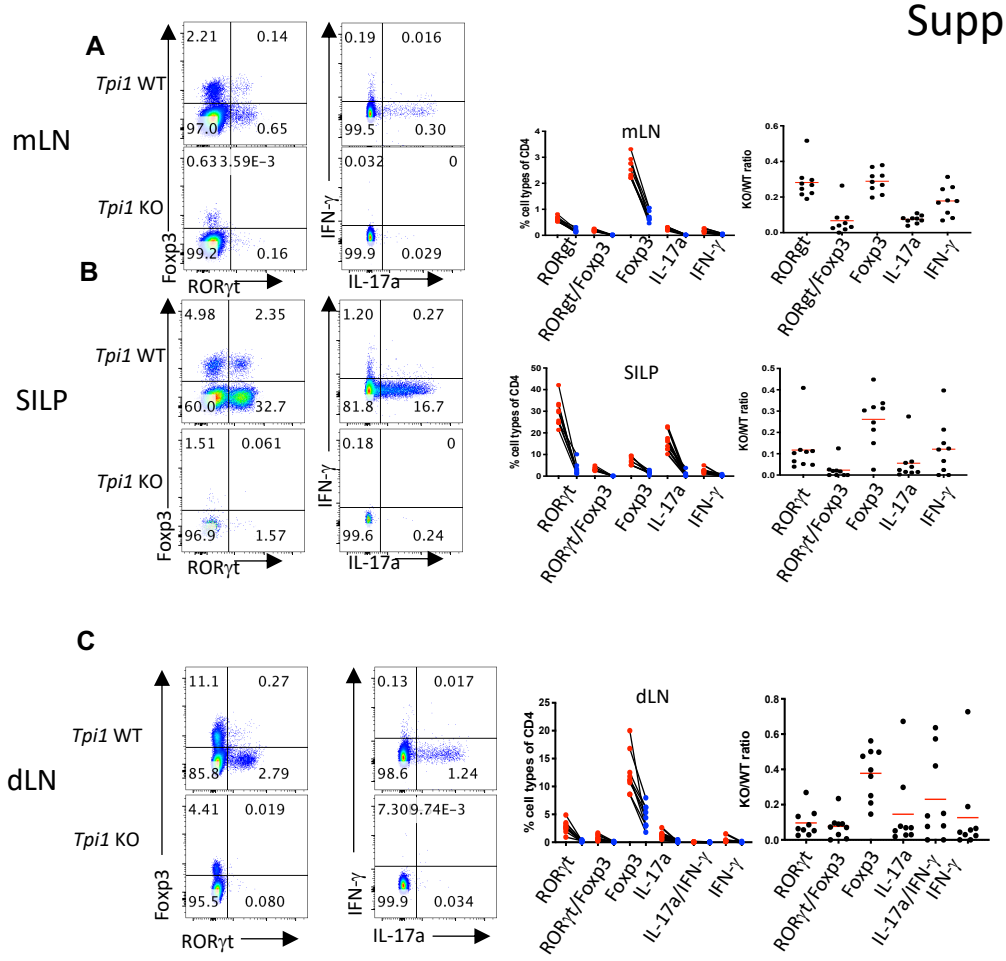

Supplementary figure 4

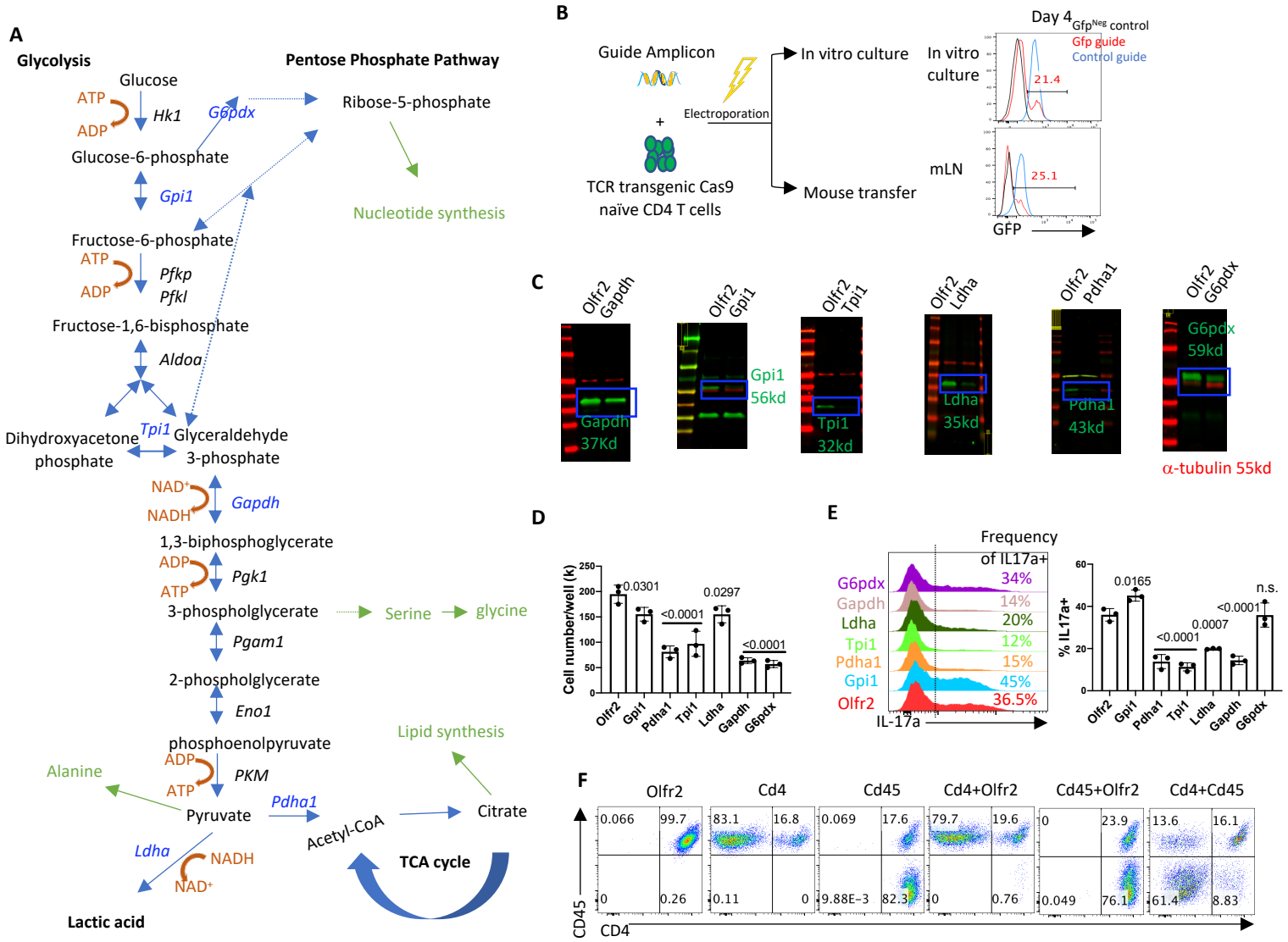

Supplementary figure 5

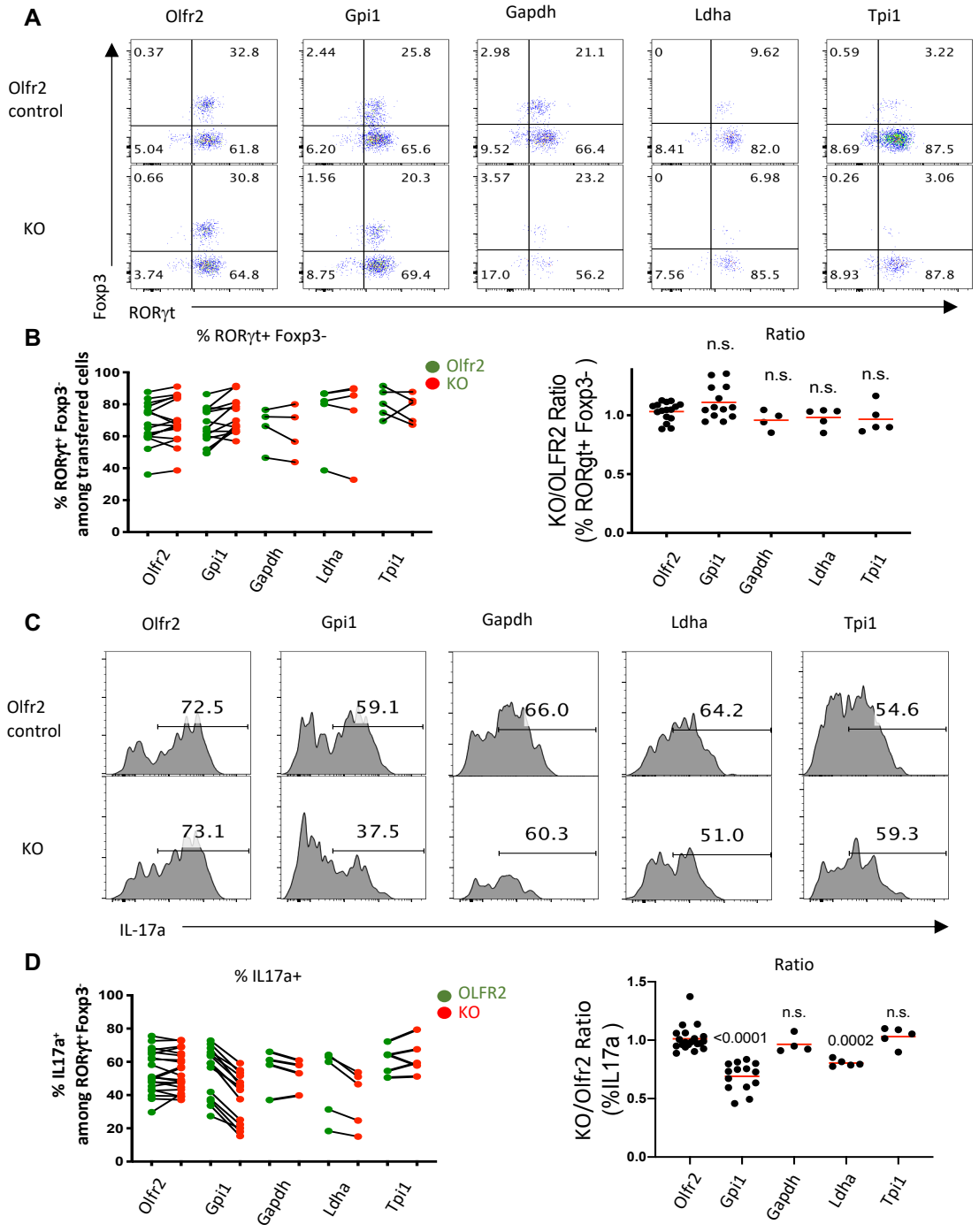
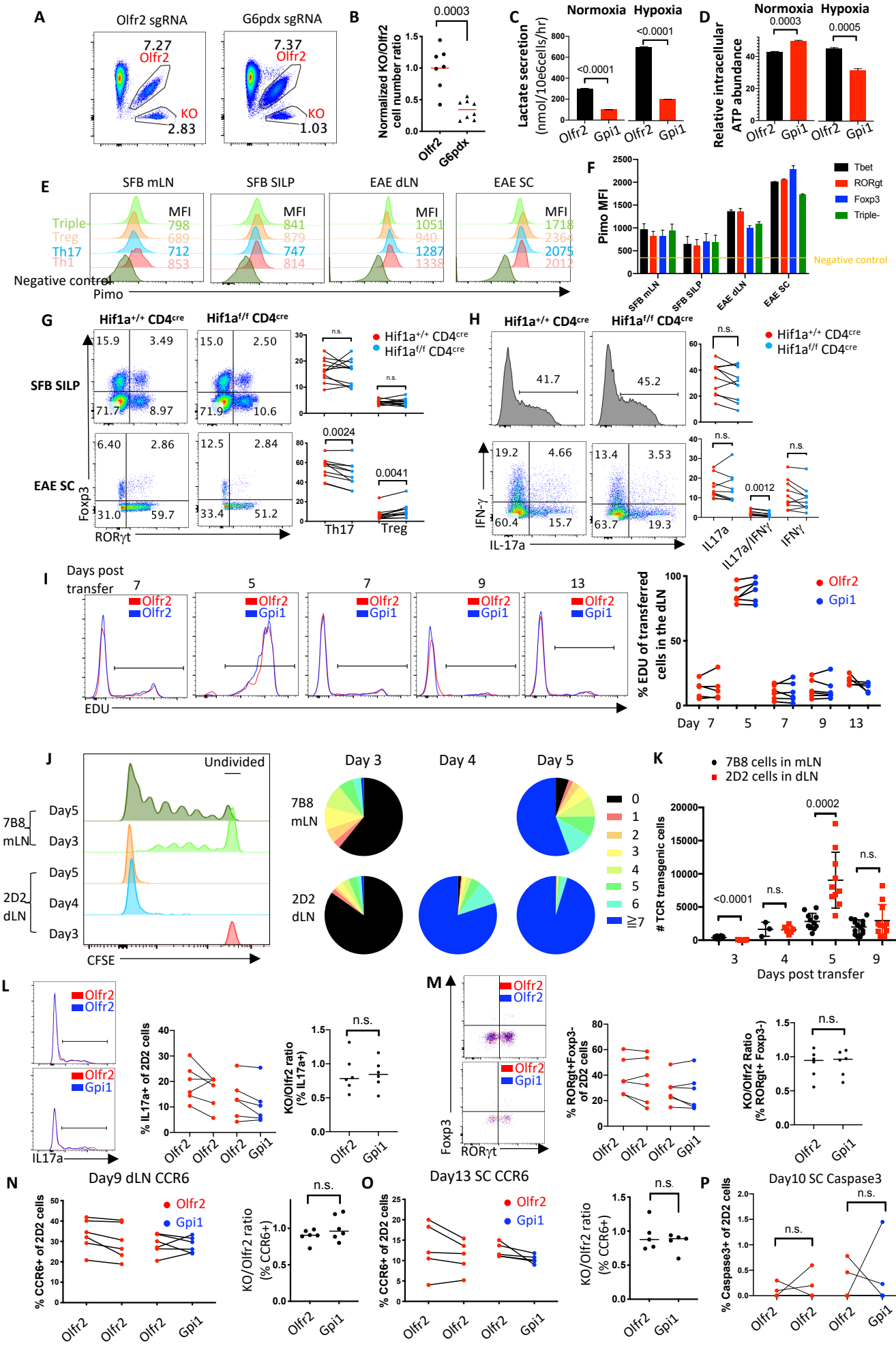
Supplementary figure 6